

Optical Properties of Soot Particles as Function of Relative Humidity

by

Boyang Zhao

A thesis submitted in partial fulfillment of the requirements for the degree of

Master of Science

Department of Chemistry
University of Alberta

© Boyang Zhao, 2020

Abstract

Optical properties, i.e. scattering coefficient and absorption coefficient, of soot aerosol particles were investigated as they restructure during a simulated atmospheric ageing process. The soot particles were generated by a McKenna burner and injected into a smog chamber after being denuded and size selected. In the smog chamber, the soot restructuring process was induced by formation of a secondary organic aerosol (SOA) coating, which was generated by the photo-oxidation reaction of the SOA precursor p-xylene with OH radical. The particle diameter, mass, scattering and absorption coefficients were monitored with a scanning mobility particle sizer, a centrifugal particle mass analyzer, and a photoacoustic extinctionsmeter, respectively. Effective density and shape factor for the particles were determined to assess the degree of restructuring. Experiments were done at different relative humidities (RH) and I found that higher RH leads to a faster restructuring process. Mass scattering cross-section, mass absorption cross-section, and mass absorption cross-section with respect to bare soot particles were calculated to show how scattering and absorption are affected by the restructuring process. Under all RH conditions, the mass scattering cross-section increased for both coated and denuded soot particles. The mass absorption cross-section with respect to bare soot particle shows an increasing trend for coated soot particles as the mass growth factor increases. High and low RH conditions give rise to a higher value of mass absorption cross-section with respect to bare soot particles compared to intermediate RH conditions (RH=40%). The mass

absorption cross-section value with respect to bare soot particles for intermediate RH is about 30% less than those for low and high RH. The overall work can provide optical information to the process of soot particles restructuring induced by SOA coating under different RH conditions.

Acknowledgments

First, I would like to thank my supervisor, Prof. Wolfgang Jäger, for all his help during my graduate studies at the University of Alberta. I really appreciate his guidance and suggestions on my research project and trouble shootings.

I also want to thank Prof. Yunjie Xu for all her suggestions about my work. It is also nice to hear a lot of interesting stories from her.

I thank my committee members, Prof. Jason Olfert and Prof. Sarah Styler, for their support on my research. I want to thank again to Prof. Jason Olfert for lending me the instruments and for his help with the calibrations.

I thank Dr. Elijah Schnitzler and Kaiser Leung for their introduction to the smog chamber system. I thank Kerry Chen, Mohsen Kazemimansh, Milad Zamani, Mario Schmidt, Ming Lyu, and Maya Abou-Ghanem for their help and suggestions regarding the instrumentation.

I thank both Wolfgang and Yunjie's group members for being my friends and colleagues. I thank my family and all my friends for their support during my studies at the University of Alberta.

I gratefully acknowledge funding from the University of Alberta.

Table of Contents

Chapter 1. Introduction	1
1.1. Aerosol and Black Carbon.....	1
1.2. Aerosol in the Atmosphere.....	2
1.3. Motivation and Outline.....	3
Chapter 2. Experimental Details	9
2.1. Experimental Setup for Soot Particle Preparation.....	9
2.2. Experimental Setup for Soot Particle Aging.....	12
2.3. Experimental Setup for Soot Particle Analysis.....	13
2.4. Calibration and Leak Tests.....	15
2.5. Description of individual components.....	16
2.5.1. The Smog Chamber.....	16
2.5.2. Electrostatic Classifier and Differential Mobility Analyzer.....	16
2.5.3. Condensation Particle Counter	17
2.5.4. Centrifugal Particle Mass Analyzer.....	17
2.5.5. Photoacoustic Extinctionmeter.....	18
2.5.5.1. Optical properties.....	18
2.5.5.2. The Symbols and Abbreviation of Optical Parameters.....	21
Chapter 3. Changes in Aerosol Optical Properties Induced by SOA Coating	26
3.1. Soot Restructuring and Morphology Change.....	27
3.2. Measurements of Absorption and Scattering Coefficients.....	32
3.2.1 Scattering.....	33
3.2.1.1 Scattering Coefficient.....	33
3.2.1.2. Mass Scattering Cross-section.....	36
3.2.2. Absorption.....	39

3.2.2.1. Absorption Coefficient.....	39
3.2.2.2. Mass Absorption Cross-section.....	41
3.2.2.3. Mass Absorption Cross-section with Respect to Mass of Bare Soot Particles.....	42
3.3. Error Discussion.....	44
Chapter 4. Conclusions.....	48
Bibliography.....	51

List of Figures

2.1. A general experimental flow chart.....	9
2.2. The experimental setup for soot sample preparation.....	10
2.3. The experimental setup for soot sample aging.....	12
2.4. The experimental setup for soot sample analysis.....	13
3.1. The change in particle diameter as function of reaction time for different relative humidities. (open circles: coated particles; solid circles: denuded particles).....	28
3.2. Diameter growth factor as function of mass growth factor at different relative humidities.....	31
3.3. Average scattering coefficient of coated soot particles as function of reaction time for different relative humidities.....	33
3.4. Average scattering coefficient of denuded soot particles as function of reaction time for different relative humidities.....	34
3.5. Scattering coefficient, particle diameter, and concentration as function of reaction time of p-xylene derived SOA.....	35
3.6. Mass scattering coefficient of denuded soot particles as function of time for different relative humidities.....	37
3.7. Mass scattering coefficient of coated soot particles as function of time for different relative humidities.....	38
3.8. Absorption coefficient of coated soot particles as function of reaction time for different relative humidities.....	40
3.9. Absorption coefficient of denuded soot particles as function of reaction time for different relative humidities.....	40
3.10. Mass absorption coefficient as function of reaction time at different relative humidities. (Hollow symbols: coated particles; solid symbols: denuded particles).....	41

3.11. Mass absorption coefficient with respect to the mass of the bare soot particles as function of mass growth factor for different relative humidities.....	43
---	----

List of Symbols

B_{abs}	Absorption coefficient
B_{sca}	Scattering coefficient
B_{ext}	Extinction coefficient
C_c	Cunningham slip correction factor
$d_{particle}$	Particle diameter
d_{ve}	Volume equivalent diameter
e	Elementary charge
i	Parameter of Mie scattering
I	Intensity
L	Distance between the sample inlet and outlet in DMA; Path length
m	Refractive index; Mass
n	Number of charges
Q_{sh}	Sheath flow rate
r	Radius of inner rod or outer cylinder for DMA and CPMA; Distance between the particle and the center of CPMA
R	Distance between particle and observer
U	Voltage
α	Size parameter
θ	Angle between scattered and incident light
λ	Wavelength
μ	Gas viscosity
ρ	Density
ρ_{eff}	Effective density
σ	Cross-section

φ	Equivalence ratio
χ	Shape factor
ω	Angular velocity
[<i>particle</i>].....	Particle number concentration

List of Abbreviations

aci.....	Aerosol-cloud interaction
ari.....	Aerosol-radiation interaction
BC.....	Black carbon
CCN.....	Cloud condensation nuclei
CPC.....	Condensation particle counter
CPMA.....	Centrifugal particle mass analyzer
CPMD.....	Counter-flow parallel-plate membrane denuder
DMA.....	Differential mobility analyzer
DOAS.....	Differential optical absorption spectroscopy
Gfd.....	Diameter growth factor
Gfm.....	Mass growth factor
MAC.....	Mass absorption cross-section
MAC(bare soot).....	Mass absorption cross-section with respect to bare soot particles
MSC.....	Mass scattering cross-section
PAX.....	Photoacoustic extinctionsmeter
PFA.....	Perfluoroalkoxy
PM.....	Particulate matter
RF.....	Radiative forcing
RH.....	Relative humidity
SMPS.....	Scanning mobility particle sizer
SOA.....	Secondary organic aerosol
SSA.....	Single scattering albedo
TD.....	Thermodenuder
VOC.....	Volatile organic compound
UV.....	Ultra-violet

Chapter 1. Introduction

I became first interested in aerosol chemistry during my time growing up in China. During my younger ages, air pollution was always a hot topic in our society. I can still remember that people tended to blame the poor air quality on the operation of heavy industries. Terms such as aerosol and $PM_{2.5}$ became first important to me during that time. In this chapter, I introduce some of the interesting properties of aerosols, including how they are characterized and their influence on our environment.

1.1. Aerosol and Black Carbon

Aerosol is defined as particles suspended in gas, and include solid and liquid phase particles.¹ The diameter of the aerosol particle is usually between 1 nm to 100 μm .² Atmospheric aerosol or atmospheric particulate matter (PM) can be categorized according to size. $PM_{2.5}$ is particulate matter with aerodynamic diameter less than or equal to 2.5 μm and PM_{10} has diameter less than or equal to 10 μm .³ PM can be quantified in terms of mass concentration, which is total mass per volume.

Aerosols in the atmosphere are mainly composed of black carbon, mineral dust, organic aerosols, and inorganic aerosols such as sea salt.⁴ In my thesis, I will mainly introduce black carbon (BC) and secondary organic aerosol (SOA).

Black carbon, also known as soot, is a well-known primary aerosol. BC is generated by incomplete combustion of burning biomass and fossil fuels.^{4,5,6} The total BC annual emission in 2007 was about 9.052 Tg, which is almost twice the emitted amount of 5.386 Tg in 1960.⁷ The lifetime of BC in the atmosphere is about a week.⁸ BC is also considered as a source of pollution and contributes to global warming.⁹ A large fraction of the world population is suffering health issues due to BC air pollution.¹⁰ It has been shown that some health issues are closer related to BC rather than $PM_{2.5}$ or PM_{10} , and BC mass concentration can be a better indicator to study these health effects.¹¹ A study on children asthma in China has indicated that

both BC and PM_{2.5} is related to this health effect, and BC is more significant.¹²

Secondary organic aerosol (SOA) is generated by oxidation of volatile organic compounds (VOCs).⁴ The VOCs can come from anthropogenic and biogenic sources. Previous studies show that biogenic sources emit more than ten times VOCs compared to anthropogenic sources and the greatest contributor are plants.¹³ Common VOCs such as α -pinene¹⁴ and xylenes^{15,16} are often used as a precursor to produce SOA in research activities. In the urban areas those aromatic precursors contribute to about one fourth of total VOCs.¹⁷

1.2. Aerosol in the Atmosphere

Exposure to aerosol may induce health effects, such as cardiac¹⁸ or lung¹⁹ disease. The aerosol size and concentration are significant factors. Aerosols in the atmosphere can also affect the global climate by scattering or absorbing incoming solar radiation. A common term to represent this is radiative forcing (RF), which is the net radiative flux change as a result of a certain climatic factor, such as atmospheric aerosol.²⁰ The unit for RF is W/m². RF describes how a factor influences Earth's energy budget. Positive RF means that Earth gains heat, which can be a factor to present global warming. Negative RF means that Earth loses heat, which will cause cooling. In the atmosphere, the most positive RF comes from carbon dioxide, which is +1.68 (+1.33 to +2.03) W/m².²⁰ The second largest contributor is methane, which RF is +0.97 (+0.74 to +1.20) W/m².²⁰

Aerosol particles in the atmosphere can directly affect the climate because they can absorb or scatter radiation from the sun and Earth.²¹ BC absorbs all visible light so it looks black to people and 'fluffy' clouds scatter all visible light so they look white.¹ As a result, aerosol particles will also cause RF. This RF can be further categorized as direct RF or aerosol-radiation interaction (ari).⁴ Particles such as mineral dust and sulfate give negative RF values, which means that scattering dominates over these particles.⁴ BC is a major component in atmospheric aerosols, and absorption is dominant. The overall contribution to RF from atmospheric BC is

positive, which is $+0.64$ ($+0.08$ to $+1.2$) W/m^2 ,^{4,20} but the uncertainty in this number is large, indicating that there is a lack of scientific understanding. The BC has two major sources, which is the combustion of biomass (RF is estimated to be $+0.03$ to $+0.4$ W/m^2) and the burning of fossil fuels and biofuels (RF is estimated to be $+0.05$ to 0.8 W/m^2).⁴

Aerosol particles can also indirectly affect the climate by acting as cloud condensation nuclei (CCN) in the atmosphere.¹⁸ CCN refers to particles that act as seeds to initiate the condensation of water vapor. These particles consist mostly of “sea salt, sulphate, sulphuric acid, nitrate, nitric acid, and some organics”.⁴ Here in this case, RF is considered as the first indirect radiative forcing or aerosol-cloud interaction (aci).⁴ The overall RF from these secondary effects is shown to be -0.7 to -1.7 W/m^2 .²² The large range is again indicative of limited scientific understanding.

What is interesting about BC is that it can absorb and scatter light, but absorption is dominant. When BC is mixed with water,²³ sulfuric acid,²⁴ or other organics,²⁵ BC can act also as a CCN. Mixing or coating of BC with these compounds can lead to a change in both scattering and absorption coefficients and therefore to a change in RF.^{23,24,25} In order to determine the contributions of scattering and absorption separately, I need to consider the scattering and absorption coefficients, which will be discussed later in Chapter 2.

1.3. Motivation and Outline

In this thesis, I describe my studies of the changes in optical properties of soot particles as a result of coating and restructuring processes under different relative humidity (RH) conditions. At the same time, I will also take morphological properties into account. Studies have shown that soot aggregates generated by a burner are formed as clusters of primary soot particles, which can undergo a restructuring process as they are coated with SOA in the atmosphere.²⁶ This restructuring process will lead to a morphological change of the soot aggregates to become more spherical.²⁶ It is known that the surface tension of the SOA coating is the main driver

of this restructuring process.²⁷ However, the SOA surface tension can be affected by ambient conditions, such as relative humidity.^{27,28} It has been shown that high RH conditions give rise to a more rapid restructuring process.²⁸ It is likely that the ability to scatter and absorb light will change during the soot restructuring process. My study will be a further step^{26,28} to study the scattering and absorption of ageing soot particles under various RH conditions. These studies will therefore contribute to an increase of our scientific understanding about the effect of soot particles on our global climate.

In Chapter 2, I introduce how I use a photo-reaction chamber (“smog chamber”) as a tool to study the ageing of the soot particles and the concurrent changes in morphology and optical properties. I explain how I prepare my samples, including clean monodisperse soot particles and SOA. I show the complete experimental scheme and describe how the instruments used for characterization work. In Chapter 3, I discuss all my experimental data. Raw data include the size, mass, scattering coefficient, and absorption coefficient throughout the whole process. Errors and possible improvements will be discussed as well. In Chapter 4, I give the overall conclusion.

References

- ¹ Hinds, W. C. Introduction. *Aerosol Technology Properties, Behavior, and Measurement of Airborne Particles*, 2nd ed.; Wiley: New York, 1999; pp. 1-14.
- ² Després, V.; Huffman, J. A.; Burrows, S. M.; Hoose, C.; Safatov, A.; Buryak, G.; Fröhlich-Nowoisky, J.; Elbert, W.; Andreae, M.; Pöschl, U.; Jaenicke, R. Primary biological aerosol particles in the atmosphere: a review. *Tellus B: Chemical and Physical Meteorology*. **2012**, *64:1*, 15598.
- ³ Schwartz, J.; Laden, F.; Zanobetti, A. The concentration-response relation between PM_{2.5} and daily deaths. *Environ. Health Perspect.* **2002**, *110*, 1025-1029.
- ⁴ Boucher, O.; Randall, D.; Artaxo, P.; Bretherton, C.; Feingold, G.; Froster, P.; Kerminen, V.-M.; Kondo, Y.; Liao, H.; Lohmann, U.; Rasch, P.; Satheesh, S. K.; Sherwood, S.; Stevens, B.; Zhang, X. Y. Clouds and aerosols. In *Climate Change 2013: The Physical Science Basis. Contribution of Working Group I to the Fifth Assessment Report of the Intergovernmental Panel on Climate Change*; Stocker, T.F.; Qin, D.; Plattner, G.-K.; Tignor, M. M.; Allen, S. K.; Boschung, J.; Nauels, A.; Xia, Y.; Bex, V.; Midgley, P. M., Eds.; Cambridge University Press: Cambridge, 2013; pp. 571-657.
- ⁵ Jacobson, M. Z. Control of fossil-fuel particulate black carbon and organic matter, possibly the most effective method of slowing global warming. *J. Geophys. Res.* **2002**, *107*, 4410.
- ⁶ Schwarz, J. P.; Gao, R. S.; Spackman, J. R.; Watts, L. A.; Thomson, D. S.; Fahey, D. W.; Ryerson, T. B.; Peischl, J.; Holloway, J. S.; Trainer, M.; Frost, G. J.; Baynard, T.; Lack, D. A.; de Gouw, J. A.; Warneke, C.; Del Nergro, L. A. Measurement of the mixing state, mass, and optical size of individual black carbon particles in urban and biomass burning emissions. *Geophys. Res. Lett.* **2008**, *35*, L13810.
- ⁷ Wang, R.; Tao, S.; Shen, H.; Huang, Y.; Chen, H.; Balkanski, Y.; Boucher, O.; Ciais, P.; Shen, G.; Li, W.; Zhang, Y.; Chen, Y.; Lin, N.; Su, S.; Li, B.; Liu, J.; Liu,

-
- W. Trend in Global Black Carbon Emissions from 1960 to 2007. *Environ. Sci. Technol.* **2014**, *48*, 6780-6787.
- ⁸ Ramanathan, V.; Carmichael, G. Global and regional climate changes due to black carbon. *Nat. Geosci.* **2008**, *1*, 221-227.
- ⁹ Bond, T. C.; Sun, H. Can reducing black carbon emissions counteract global warming? *Environ. Sci. Technol.* **2005**, *39*, 5921-5926.
- ¹⁰ Menon, S.; Hansen, J.; Nazarenko, L.; Luo, Y. Climate effects of black carbon aerosols in China and India. *Science.* **2002**, *297*, 2250-2253.
- ¹¹ Janssen, N. A. H.; Gerlofs-Nijland, M. E.; Lanki, T.; Salonen, R. O.; Cassee, F.; Hoek, G.; Fischer, P.; Brunekreef, B.; Krzyzanowski, M. Health effects of black carbon. World Health Organization: Copenhagen, Denmark, 2012.
- ¹² Hua, J.; Yin, Y.; Peng, L.; Du, L.; Geng,; Zhu. L. Acute effects of black carbon and PM_{2.5} on children asthma admissions: a time-series study in a Chinese city. *Sci. Total Environ.* **2014**, *481*, 433-438.
- ¹³ Atkinson, R.; Arey, J. Atmospheric degradation of volatile organic compounds. *Chem. Rev.* **2003**, *103*, 4605-4638.
- ¹⁴ Zhang, X.; McVay, R. C.; Huang, D. D.; Dalleska, N. F.; Aumont, B.; Flagan, R. C.; Seinfeld, J. H. Formation and evolution of molecular products in α -pinene secondary organic aerosol. *PNAS.* **2015**, *112*, 14168-14173.
- ¹⁵ Ng, N. L.; Kroll, J. H.; Chan, A. W. H.; Chhabra, P. S.; Flagan, R. C.; Seinfeld, J. H. Secondary organic aerosol formation from m-xylene, toluene, and benzene. *Atmospheric Chemistry and Physics Discussions*, European Geosciences Union, **2007**, *7*, 4085-4126.
- ¹⁶ Huang, M.; Zhang, W.; Hao, L.; Wang, Z.; Zhao, W.; Gu, X.; Fang, L. Low-molecular weight and oligomeric components in secondary organic aerosol from the photooxidation of p-xylene. *J. Chin. Chem. Soc.* **2008**, *55*, 456-463.

-
- ¹⁷ Healy, R. M.; Temime, B.; Kuprovskyte, K.; Wenger, J. C. Effect of relative humidity on gas/particle partitioning and aerosol mass yield in the photooxidation of p-xylene. *Environ. Sci. Technol.* **2009**, *43*, 1884-1889.
- ¹⁸ Hu, Z. Spatial analysis of MODIS aerosol optical depth, PM_{2.5}, and chronic coronary heart disease. *Int. J. Health Geogr.* **2009**, *8*, 27.
- ¹⁹ Tie, X.; Wu, D.; Brasseur, G. Lung cancer mortality and exposure to atmospheric aerosol particles in Guangzhou, China. *Atmos. Environ.* **2009**, *43*, 2375-2377.
- ²⁰ Myhre, G.; Shindell, D.; Bréon, F.-M.; Collins, W.; Fuglestvedt, J.; Huang, J.; Koch, D.; Lamarque, J.-F.; Lee, D.; Mendoza, B.; Nakajima, T.; Robock, A.; Stephens, G.; Takemura, T.; Zhang, H. Anthropogenic and natural radiative forcing. In *Climate Change 2013: The Physical Science Basis. Contribution of Working Group I to the Fifth Assessment Report of the Intergovernmental Panel on Climate Change*; Stocker, T.F.; Qin, D.; Plattner, G.-K.; Tignor, M. M.; Allen, S. K.; Boschung, J.; Nauels, A.; Xia, Y.; Bex, V.; Midgley, P. M., Eds.; Cambridge University Press: Cambridge, 2013; pp. 659-740.
- ²¹ Lohmann, U.; Feichter, J. Global indirect aerosol effects: a review. *Atmos. Chem. Phys.* **2005**, *5*, 715-737.
- ²² Takemura, T.; Nozawa, T.; Emori, S.; Nakajima, T. Y.; Nakajima, T. Simulation of climate response to aerosol direct and indirect effects with aerosol transport-radiation model. *J. Geophys. Res.* **2005**, *110*, D02206.
- ²³ Liu, L.; Mishchenko, M. I.; Menon, S.; Macke, A.; Lacis, A. A. The effect of black carbon on scattering and absorption of solar radiation by cloud droplets. *J. Quant. Spectrosc. Radiat. Transfer.* **2002**, *74*, 195-204.
- ²⁴ Khalizov, A. F.; Xue, H.; Wang, L.; Zheng, J.; Zhang, R. Enhanced light absorption and scattering by carbon soot aerosol internally mixed with sulfuric acid. *J. Phys. Chem. A.* **2009**, *113*, 1066-1074.

-
- ²⁵ Xue, H.; Khalizov, A. F.; Wang, L.; Zheng, J.; Zhang, R. Effects of dicarboxylic acid coating on the optical properties of soot. *Phys. Chem. Chem. Phys.* **2009**, *11*, 7869-7875.
- ²⁶ Schnitzler, E. G.; Dutt, A.; Charbonneau, A. M.; Olfert, J. S.; Jäger, W. Soot aggregate restructuring due to coatings of secondary organic aerosol derived from aromatic precursors. *Environ. Sci. Technol.* **2014**, *48*, 14309-14316.
- ²⁷ Schnitzler, E. G.; Gac, J. M.; Jäger, W. Coating surface tension dependence of soot aggregate restructuring. *J. Aerosol Sci.* **2017**, *106*, 43-55.
- ²⁸ Leung, K. K.; Schnitzler, E. G.; Jäger, W.; Olfert, J. S. Relative humidity dependence of soot aggregate restructuring induced by secondary organic aerosol: effects of water on coating viscosity and surface tension. *Environ. Sci. Technol. Lett.* **2017**, *4*, 386-390.

Chapter 2. Experimental Details

In this chapter, I will describe the detailed setup for my project. The instruments used to characterize aerosol particle properties, including optical ones, and their operating principles, will be introduced in detail. I will also provide information about when and how to calibrate these instruments. An overall experimental flow chart is shown below in Figure 2.1.



Figure 2.1. A general experimental flow chart.

The experimental process can be divided into three major steps. In the beginning, soot particles will be produced using a laboratory burner. After removing contaminants followed by particle size selection, the soot particles will be introduced into a smog chamber. Second, a photochemical reaction is initiated inside the smog chamber to produce secondary organic aerosol (SOA), which will coat the soot particles and induce the soot aging process. Finally, the aged soot particles will be analyzed in terms of soot morphology and optical properties.

2.1. Experimental Setup for Soot Particle Preparation

The experimental scheme for soot particle preparation is shown below in Figure 2.2.

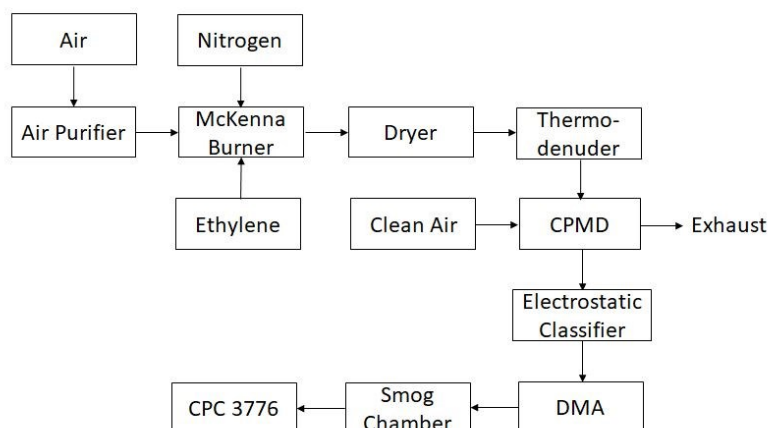


Figure 2.2. The experimental setup for soot sample preparation.

A McKenna burner is my tool to generate the soot particles. Clean air and ethylene are used as fuel and nitrogen is used as an inert carrier gas. The sample stream from the burner then flows through a dryer to remove water, a thermodenuder (TD) to evaporate the semi-volatile compounds, and a counter-flow parallel-plate membrane denuder (CPMD) to remove those volatile organic compounds (VOCs). At this point, I will have bare soot particles without any contaminants, but with a wide size range. In order to obtain a sample of monodisperse soot particles, the sample stream enters an electrostatic classifier (TSI; model 3080) which contains a differential mobility analyzer (DMA, TSI; model 3081) to select particle size. The size-selected soot then enters our smog chamber, and the soot number concentration is monitored using a condensation particle counter (CPC, TSI; model 3776).

The McKenna burner is a widely used burner to generate soot particle, which will premix the fuel and air to give a reproducible flame.^{1,2} Since the laboratory air has a particle concentration of about 3000 to 8000 particles/cm³, which is much too high of a background concentration, a pure air generator (AADCO; 737-series), i.e. an air purifier, is used.

To operate the McKenna burner, cooling water has to pass through the tubes

inside the sintered bronze burning plug on top of the burner.³ Nitrogen gas and cold water need to be turned on before applying fuels.

In previous work done by Dr. Schnitzler,⁴ soot particles were produced with a McKenna Burner by mixing 1.1 slpm ethylene and 8 slpm zero air. The equivalence ratio ϕ can be calculated by Equation (2.1)

$$\phi = \frac{\left(\frac{Fuel}{Air}\right)_{actual}}{\left(\frac{Fuel}{Air}\right)_{stoic}} \quad (2.1)$$

Here, $\left(\frac{Fuel}{Air}\right)_{actual}$ and $\left(\frac{Fuel}{Air}\right)_{stoic}$ mean the actual and stoichiometric fuel/air ratios, respectively.

For each mole of ethylene, 3 mole of oxygen are required to achieve complete reaction. For each mole of oxygen, there will be 3.76 mole of nitrogen accompanying with it in air. The calculated equivalence ratio is 2.

However, currently the burner cannot generate enough soot particles at our desired diameter at an equivalence ratio of 2, which is likely a result of partial blockage of the porous metal plug in the McKenna burner. I noticed that the soot concentration generated by the McKenna burner has decreased, which makes it difficult to fill up the smog chamber to a soot particle concentration of 1000 particles/cm³. As a result, I decided to increase the equivalence ratio by increasing the air supply to 8.43 slpm and increasing the ethylene supply to 1.34 slpm. This gives an equivalence ratio of 2.27.

The soot particles generated by the McKenna burner pass through a calcium sulfate containing diffusion dryer, made by a former group member, to remove water. This is followed by a thermodenuder, heated up to 300K, in order to evaporate any volatile organic components, which are removed in a CPMD.⁵

The next step is to select soot particle size, so I need to connect an electrostatic classifier with a DMA column attached. In an electrostatic classifier large particles are removed first with an impactor and a reproducible particle charge distribution is achieved with an aerosol neutralizer, which contains an X-ray source (TSI; Model

3087). A DMA is a device to select particles with a specific size by balancing drag force and electrical force of the charged particles in a sheath flow. I will provide details later in this chapter. The sheath flow of the electrostatic classifier needs to be adjusted to achieve a sheath to sample flow ratio of 3. All my experiments were done on soot aggregates of 250 nm diameter and these are injected into the smog chamber. According to my observation, the full width at half maximum for the classified size distribution is about 40 nm. Initially, the perfluoroalkoxy (PFA) bag in the smog chamber needs to be filled up with clean air from the air purifier to minimize the particle background concentration. The background particle concentration in the bag should be less than 50 particles/cm³. The soot particle concentration is monitored using a CPC (TSI; model 3776) and the soot injection is stopped when the concentration reaches about 1000 particles/cm³.

2.2. Experimental Setup for Soot Particle Aging

The experimental scheme for soot aging is shown below in Figure 2.3.

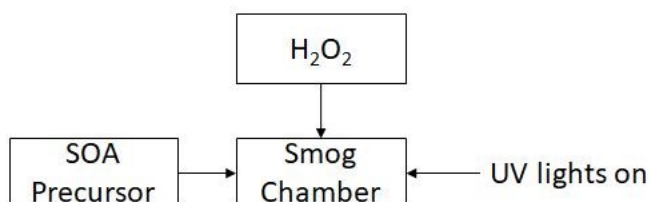


Figure 2.3. The experimental setup for soot sample aging.

After the soot particle preparation stage, the smog-chamber contains a sample of monodisperse soot particles of 250 nm diameter at a concentration of about 1000 particles/cm³. In order to initiate the aerosol particle aging process, I induce a photochemical reaction to form SOA. A SOA precursor and hydrogen peroxide are added into the chamber. Once the desired concentration is reached, the UV lights are switched on to start the photo-chemical SOA forming reaction.

There have been many earlier studies on restructuring of soot aggregates upon

coating with SOA.^{4,6,7} The SOA precursor is a VOC, which is introduced into the chamber through a bubbler. In my experiment, p-xylene (Fisher, 99.9% purity) is utilized as the SOA precursor. The p-xylene concentration in the smog-chamber is monitored by a differential optical absorption spectroscopy (DOAS) system. Hydroxyl (OH) radicals, ozone, and NO_x are often used as oxidizing agent to form SOA.⁸ Since oxidation of aromatic VOCs with OH radical results often in good SOA yields,⁸ OH radical was selected and produced by photolysis of hydrogen peroxide (H₂O₂) upon irradiation with UV light. The hydrogen peroxide is injected through a syringe into the smog chamber. Before the actual experiments, I have used different amounts of p-xylene and H₂O₂ for preliminary tests. Eventually, 0.5 ppm of p-xylene and 0.5 ml of H₂O₂ was used because this condition leads to a reasonable reaction rate for me to monitor the soot aggregate restructuring over a total experiment time of approximately eight hours.

2.3. Experimental Setup for Soot Particle Analysis

The experimental scheme for the soot particle analysis is shown below in Figure 2.4.

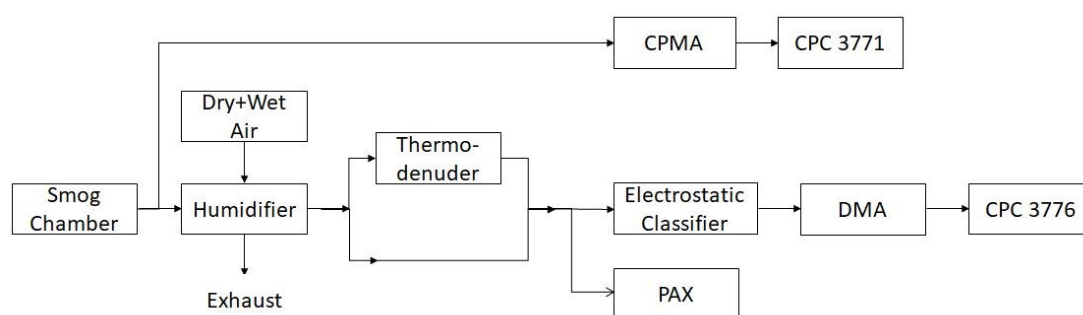


Figure 2.4. The experimental setup for soot sample analysis.

The SOA production begins with switching on the UV lights. This point in time

marks time zero for all my measurements. As SOA is produced it condenses onto the soot particles and induces the soot restructuring process. The soot particles are characterized throughout this restructuring process in terms of the soot morphology using a centrifugal particle mass analyzer (CPMA, Cambustion Ltd), a DMA (TSI; model 3081), and two CPCs (TSI; models 3771 and 3776) and optical properties using a photoacoustic extinctionsmeter (PAX, Droplet Measurement Technologies, Inc.; model 870 nm).

Sample from the smog chamber is extracted at a rate of 2.3 slpm and runs through two instrument arms. One of them is used to measure the particle mass with a CPMA, which can measure masses down to the femtogram level.⁹ The CPMA is coupled to a CPC 3771 to give the mass distribution throughout the experiment.

In the other arm, particle size and optical properties are determined of the soot particles with or without SOA coating and at different relative humidities. The soot sample passes through a Nafion membrane humidifier (Perma Pure; PD-265-24SS). A mixture of wet and dry air feeds into the Nafion tube to create the desired relative humidity (RH) condition. The RH is measured with a RH sensor (Sensirion; SHT75). The sample flow in this arm is 1.3 slpm, so the residence time of the aggregates is sufficient to complete the restructuring.¹⁰ After the humidifier, the sample path splits again into two arms. One of the paths includes a thermodenuder to remove the SOA coating and the other path will keep the SOA coating. A DMA coupled to a CPC 3776, i.e. a scanning mobility particle sizer (SMPS), is then deployed to obtain the size distribution.

At the same time, a PAX is collecting data for the soot particle optical properties. A PAX is a device that contains a photoacoustic cell to measure absorption and a reciprocal nephelometer to measure scattering simultaneously. An 870 nm laser is used for the PAX, because black carbon is favored in this region.

The functioning of CPMA, PAX, and CPC will be discussed in detail later in this chapter.

2.4. Calibration and Leak Tests

On October 11, 2018, a leak test on the electrostatic classifier was performed according to the instructions in the instrument manual.¹¹ Calibrations on sheath, bypass, and aerosol flows were done separately. For each check, the classifier was turned on and the respective pathway isolated. The pathway was evacuated until a pressure of about 100 mbar was reached. The pump was then isolated from the pathway and a pressure reading was taken after a waiting time of 5 minutes. The pressure is allowed to increase by 3.4 mbar (0.1 inHg).¹¹ The pressure was read by a built-in pressure sensor in the classifier.

Voltage calibrations of the inner rod for the DMA, between 10V to 1000V, and the CPMA, between 0.1V to 1000V, were done in the workshop in the Mechanical Engineering Building on October 12, 2018. This process took place under the instruction of Dr. Olfert. For voltage higher than 1V, the errors are within 5%. The test on the performance of the CPMA was done by tandem of DMA, CPMA, and CPC 3776 on October 2, 2018. A sample of bis(2-ethylene) sebacate particles, with a density of 900 kg/cm³, were generated by an atomizer. The DMA selects particles with a certain diameter, and the CPMA and CPC 3776 provide scans of the mass distribution. For particles of different sizes, the calculated densities are about 840 kg/cm³. The error is 6.7%, which is acceptable.

A Gilian Gilibrator-2 NIOSH primary standard air flow calibrator (bubble flow meter) was used to calibrate the sheath-air flow, which means the built-in sheath flow meter, ranging from 2 slpm to 18 slpm, inside the classifier. The errors are within 5%. A set flow test was also carried on by a bubble flow meter. The set values on the CPC 3776 are 0.3 slpm and 1.5 slpm; on the CPC 3771 is 1.0 slpm; and on the CPMA is 1.0 slpm. The errors are within 5%. These calibrations were all done on October, 2018.

The inlet, exhaust, and the ethylene flow meters were calibrated using a bubble flow meter. The last calibration date was February 21, 2019. Since the readings for these flow meters varied from the previous time, I recommend that the calibration

should be carried out once a year.

Calibration and clean-up of the PAX were done in Dr. Olfert's laboratory by Mohsen Kazemimanesh.

2.5. Description of individual components

2.5.1. The Smog Chamber

A smog chamber is used to simulate atmospheric conditions with controlled parameters. In my work, I used the smog-chamber to study the morphology changes, and accompanying changes in optical properties, of soot particles upon aging in the atmosphere.¹² The smog chamber in our laboratory consists of a 1.8 m³ perfluoroalkoxy film bag, which is placed inside an aluminum housing. It is suspended on two of the upper edges such that it is placed in the center of the aluminum housing. The bag is surrounded by 24 UV lights with emission peak at 350 nm and power of 32W. There are three fans located on the top and bottom inside the chamber. Temperature sensors are also contained around the bag.

2.5.2. Electrostatic Classifier and Differential Mobility Analyzer

The electrostatic classifier contains an impactor and an aerosol neutralizer (TSI; model 3087). The impactor has an impaction plate perpendicular to a nozzle, which will create an angle when particles enter through the gas stream. Large size particle will hit the impaction plate due to the large radius terms for centrifugal force. The remaining particles will be allowed to pass this right angle.

Aerosol particles carry electrostatic charges after generation and an aerosol neutralizer is used to produce a predictable charge distribution in which most particles carry a single charge. This is required because the subsequent DMA selects a specific particle size by balancing electrical force and drag force. The DMA has an inner rod connected to a high negative electric potential. When a positively charged particle flowing through the gas stream, it will experience a drag force on the opposite direction. This will create unique trajectory inside the DMA column, which only

depends on the hydrodynamic size of the particle.

This particle diameter, $d_{particle}$, can then be determined using Equation (2.2).¹¹

$$\frac{d_{particle}}{C_c(d_{particle})} = \frac{2neUL}{3\mu Q_{sh} \ln\left(\frac{r_2}{r_1}\right)} \quad (2.2)$$

Here, n is the number of charges, e is elementary charge, $C_c(d_{particle})$ is the Cunningham slip correction factor in terms of $d_{particle}$, the diameter of particle, μ is the gas viscosity, Q_{sh} and is the sheath flow rates, U is the voltage of the inner rod, L is the distance between the sample inlet and outlet, r_1 is the radius of inner rod, r_2 is the radius of the DMA column.

Here, Q_{sh} and U are adjustable variables. Based on Equation (2.2), we can solve for the particle diameter, $d_{particle}$, which means that only particles within a certain range of diameters can pass through the DMA.

2.5.3. Condensation Particle Counter

The CPC is a device to measure concentrations of particles in small size range down to 10 nm for CPC 3771¹³ or 2.5 nm for CPC 3776.¹⁴ Particles entering the CPC will visit a heat saturator, where n-butanol is evaporated. When the particle stream passes through, it will carry the supersaturated gaseous n-butanol into the following cooled condenser. The gaseous n-butanol will undergo heterogeneous nucleation onto the particle, which increases the particle size. This process will make the particle large enough to be detected by interrupting the beam of a laser diode.^{13,14}

2.5.4. Centrifugal Particle Mass Analyzer

The CMPA is a device to measure particle mass. Inside the CPMA classifier, there is an outer cylinder at a high positive voltage and an inner rod at a negative voltage. During operation, inner rod and outer cylinder rotate with different angular velocities and the particle inside experiences a centrifugal force towards the outer cylinder. The larger angular velocity for the inner rod compared to the outer cylinder creates a velocity profile in the angular direction that decreases from the inner rod to the outer

cylinder.^{15,16} This will cancel the influence of the position at which particles enter the classifier.

Since the soot particle has already been charged by the aerosol neutralizer before injection to the chamber, the particle will also experience an electrical force in the opposite direction, i.e. towards the inner rod. Similarly to a DMA, balancing of centrifugal force and electrostatic force will create unique trajectory inside the cylinder. Since the electrical force and centrifugal force are perpendicular to the moving direction of the particle, the drag force does not enter the consideration. As a result, the trajectory only depends on the mass, m , of the particle.

Inside the classifier, the mass is selected based on Equation (2.3).¹⁵

$$m = \frac{neU}{\omega^2 r^2 \ln\left(\frac{r_2}{r_1}\right)} \quad (2.3)$$

Here, n is the number of charges, e is elementary charge, U is the voltage of the outer surface, r is the position between the particle and the center of inner cylinder (which is usually considered as the center between inner and outer cylinder), ω is the angular velocity at position r , r_1 is the radius of inner cylinder, r_2 is the radius of outer cylinder.

2.5.5. Photoacoustic Extinctionmeter

This is the first time a PAX is used in our laboratory and since it is a critical instrument for my MSc work, I will provide some information about this device.

2.5.5.1. Optical properties

When light hits a particle or a medium, it has a chance to be scattered or absorbed. The extinction of light is the sum of scattering and absorption. It can be calculated from the incoming and transmitted radiation. The scattering and absorption coefficients are a measure of the ability of a medium to scatter or absorb light.

The sum of absorption and scattering coefficients is known as extinction coefficient, which is given by Equation (2.4).

$$B_{ext} = B_{sca} + B_{abs} \quad (2.4)$$

The extinction of light is can be calculated according to the Beer-Lambert law given in Equation (2.5).¹⁷

$$\ln \frac{I_0}{I_T} = B_{ext} L \quad (2.5)$$

Here, I_0 is the intensity of the incident light, I_T is the intensity of transmitted light, B_{ext} is the extinction coefficient, and L is the path length. The extinction coefficient is a measure of the total attenuation of light when it passes through a medium.

The absorption coefficient, B_{abs} , can be defined as the imaginary part of a material's refractive index.¹⁷ A material that does not absorb light will have a zero imaginary part of the refractive index.

Scattering is a little more complicated compared to absorption. By solving the Maxwell equation, Mie has determined the intensity of electromagnetic radiation by a particle as function of scattering angle.¹⁸ If the particle diameter is much less than the wavelength of the incident light, Rayleigh scattering is a good approximation. The intensity of the scattered light is given by Equation (2.6).¹⁷

$$I_R = I_0 \frac{\pi^4 d_{particle}^6}{8R^2 \lambda^4} \left(\frac{m^2 - 1}{m^2 + 2} \right)^2 (1 + \cos^2 \theta) \quad (2.6)$$

Here, I_R is the intensity of Rayleigh scattered light, I_0 is the intensity of incident light, $d_{particle}$ is the particle diameter, R is the distance from the particle, λ is the wavelength of the incident light, m is the refractive index, and θ is the angle between scattered and incident light.

For simplicity, the term $\frac{\pi d p}{\lambda}$ is usually defined as size parameter, α .¹⁷

A classic application of Equation (2.6) is to explain why the sky is blue. Based on Equation (2.6), we know that the I_R is proportional to the inverse fourth power of λ . So, the scattered light intensity is dominated by the short wavelengths of the incident radiation. Since blue light has shorter wavelength than red light, I_R for blue light will be greater than for red light. During sun set on the other hand, the sun light travels a long distance through the atmosphere, and much of the blue light scatters away. In this case, mostly red light remains and can be seen on the ground.

According to the angular term $(1 + \cos^2 \theta)$, I_R in the forward ($\theta=0$) and backward ($\theta=\pi$) directions is 1.5 time larger than I_R in the perpendicular direction ($\theta=\frac{\pi}{2}$).

When the particle diameter is close to the wavelength of the incident light, it undergoes Mie scattering. The intensity of the Mie scattered light, I_M , is given in Equation (2.7).^{17,19}

$$I_M = I_0 \frac{\lambda^2}{8\pi^2 dp^2} (i_1 + i_2) \quad (2.7)$$

Here, I_M is the intensity of Mie scattered light, i_1 and i_2 are parameters of Mie scattering related to perpendicular and parallel polarization with respect to the refractive index, size parameter, and angle between scattered and incident light. Unfortunately, the terms i_1 and i_2 involve complicated mathematics of derivation,^{19,20} which is difficult to show all in this thesis. In general, the pattern in the Mie scattering regime is related to the size parameter,¹⁸ and it will always have a greater scattering light intensity in the forward direction.

The scattering coefficient, B_{sca} , for Mie scattering can be written as an infinite series, which includes size parameter, refractive index, spherical Bessel functions of the first kind, and spherical Hankel functions.^{19,20,21}

The PAX is used to measure the scattering coefficient, B_{sca} , and the absorption coefficient, B_{abs} , of aerosol particles simultaneously. Measurements can be taken once every second. The on-board computer of the PAX instrument also calculates the extinction coefficient, B_{ext} , by Equation (2.4) and the single scattering albedo (SSA) by Equation (2.8) and includes those data automatically in the output file.

$$SSA = \frac{B_{sca}}{B_{ext}} \quad (2.8)$$

SSA is a parameter that describes the contribution of scattering to the overall extinction

In the PAX instrument, the sample flow is split into two pathways. The absorption coefficient is measured by a photoacoustic cell and the scattering coefficient is measured by a reciprocal nephelometer. The output of an 870 nm laser

passes through these two devices so that absorption and scattering coefficients can be measured simultaneously.²² A photoacoustic cell is a device that detects pressure waves generated during a light absorption event. When a laser beam hits the soot sample, it heats up, expands, and generates a pressure wave which is detected by a microphone.²³ A nephelometer is a device that measures scattering. When the laser beam hits the particle, the scattered light intensity is measured by a detector which is installed at 90 degrees to the laser beam.²⁴ A photodiode is used as the light detector.

Before each measurement, the PAX needs a warm-up time of at least one hour.²² Since I am analyzing soot particles, there is a possibility that soot particles can accumulate and block the laser beam path, for example, by sticking onto the mirrors. This process is difficult to prevent, so I need to check the laser intensity during the warm-up. The laser intensity should be no less than 650 mW, as described on the “Alarm Page” in the PAX manual.²² If the laser power is less than 650 mW, I need to bring the PAX to Dr. Mohsen Kazemimanesh to clean the mirrors. To ensure that the PAX measurements are synchronized with SMPS and CPMA scans, I adjust the Set Zero Interval in the PAX menu to be 240 seconds. There will be a fixed 70-second zeroing time, including 20 seconds of flushing air, 30 seconds of zeroing, and another 20 seconds of flushing. In the remaining 170 seconds, the PAX performs a measurement every second. Consequently, during this measurement cycle, the PAX acquires 170 individual data points.

2.5.5.2. The Symbols and Abbreviation of Optical Parameters

One of the first things that come to my mind when I read optics related papers is that quite a few symbols are not used uniformly, or one parameter can be denoted by many different labels. For example, σ is used to represent cross-section²⁵ in some instances or mass cross-section²³ in others.

Here, in my thesis, I use the symbol B , as in B_{abs} , for coefficients. I use the abbreviation to denote mass cross-sections, such as MAC for mass absorption cross-section. The cross-section, σ , is defined as a coefficient over number

concentration of the sample, but I will not include this term in my thesis. The unit for coefficient is m^{-1} or Mm^{-1} . The unit for cross-section is m^2 . The unit for mass cross-section is m^2/g . I have noticed that the symbols or abbreviation of coefficient, cross-section, and mass cross-section are quite confusing throughout the literature. So, the simple way I use to distinguish them is by identifying their units.

References

- ¹ Migliorini, F.; De Iulii, S.; Cignoli, F.; Zizak, G. How “flat” is the rich premixed flame produced by your McKenna burner? *Combust. Flame*. **2008**, *153*, 384-393.
- ² Olofsson, N. -E.; Bladh, H.; Bohlin, A.; Johnsson, J.; Bengtsson, P, -E. Are sooting premixed porous-plug burner flames one-dimensional? A laser-based experimental investigation. *Combust. Sci. Technol.* **2013**, *185*, 293-309.
- ³ Burners. <http://www.flatflame.com/burner-description.html> (accessed Feb 19, 2020).
- ⁴ Schnitzler, E. G.; Dutt, A.; Charbonneau, A. M.; Olfert, J. S.; Jäger, W. Soot aggregate restructuring due to coatings of secondary organic aerosol derived from aromatic precursors. *Environ. Sci. Technol.* **2014**, *48*, 14309-14316.
- ⁵ Ruiz, P. A.; Lawrence, J. E.; Ferguson, S. T.; Wolfson, J. M.; Koutrakis, P. A counter-current parallel-plate membrane denuder for the non-specific removal of trace gases. *Environ. Sci. Technol.* **2006**, *40*, 5058-5063.
- ⁶ Qiu, C.; Khalizov, A. F.; Zhang, R. Soot aging from OH-initiated oxidation of toluene. *Environ. Sci. Technol.* **2012**, *46*, 9464-9472.
- ⁷ Guo, S.; Hu, M.; Lin, Y.; Gomez-Hernandez, M.; Zamora, M. L.; Peng, J.; Collins, D. R.; Zhang, R. OH-Initiated oxidation of m-xylene on black carbon aging. *Environ. Sci. Technol.* **2016**, *50*, 8605-8612.
- ⁸ Gao, G.; Jang, Myoseon. Effects of particle acidity and UV light on secondary organic aerosol formation from oxidation of aromatics in the absence of NO_x. *Atmos. Environ.* **2007**, *41*, 7603-7613.
- ⁹ Kuwata, M. Particle classification by the tandem differential mobility analyzer-particle mass analyzer system. *Aerosol Sci. Technol.* **2015**, *49*, 508-520.
- ¹⁰ Leung, K. K.; Schnitzler, E. G.; Jäger, W.; Olfert, J. S. Relative humidity dependence of soot aggregate restructuring induced by secondary organic aerosol: effects of water on coating viscosity and surface tension. *Environ. Sci. Technol. Lett.* **2017**, *4*, 386-390.

-
- ¹¹ TSI Incorporated. Series 3080 Electrostatic Classifier, Operation and Service manual. **2009**.
- ¹² Wu, S.; Lü, Z.; Hao, J.; Zhao, Z.; Li, J.; Takekawa, H.; Minoura, H.; Yasuda, A. Construction and characterization of an atmospheric simulation smog chamber. *Adv. Atmos. Sci.* **2007**, *24*, 250-258.
- ¹³ TSI Incorporated. Model 3771/3772 Condensation Particle Counter, Operation and Service manual. **2007**.
- ¹⁴ TSI Incorporated. Model 3776 Ultrafine Condensation Particle Counter, Operation and Service manual. **2006**.
- ¹⁵ Olfert, J. S.; Reavell, S. StJ.; Rushton, M. G.; Collings, N. The experimental transfer function of the Couette centrifugal particle mass analyzer. *J. Aerosol Sci.* **2006**, *37*, 1840-1852.
- ¹⁶ Olfert, J. S. A numerical calculation of the transfer function of the Fluted centrifugal particle mass analyzer. *Aerosol Sci. Technol.* **2005**, *39*, 1002-1009.
- ¹⁷ Hinds, W. C. Optical Properties. *Aerosol Technology Properties, Behavior, and Measurement of Airborne Particles*, 2nd ed.; Wiley: New York, 1999; pp. 349-378.
- ¹⁸ Pu, Y.; Chen, J.; Wang, W.; Alfano, R. R. Basic optical scattering parameter of the brain and prostate tissues in the spectral range of 400-2400 nm. *Neurophotonics and Biomedical Spectroscopy*. **2019**, 229-252.
- ¹⁹ Grainger, R. G.; Lucas, J.; Thomas, G. E.; Ewen, G. B. L. Calculation of Mie derivatives. *Appl. Opt.* **2004**, *43*, 5386-5393.
- ²⁰ Bohren, C. F.; Huffman, D. R. Absorption and scattering by a sphere. *Absorption and Scattering of Light by Small Particles*. Wiley: New York, 1998; pp. 83-129.
- ²¹ Cox, A.J.; DeWeerd, A. J.; Linden, J. An experiment to measure Mie and Rayleigh total scattering cross section. *Am. J. Phys.* **2002**, *70*, 620-625.
- ²² Droplet Measurement Technologies. Photoacoustic extinctionmeter operator manual. **2014**.

-
- ²³ Ismail, A. F.; Khulbe, K. C.; Matsuura, T. RO membrane characterization. *Reverse Osmosis*. Elsevier Inc., 2019; pp. 57-90.
- ²⁴ Queensland; c=A. U. o=T. S. of. Measuring visibility.
<https://www.qld.gov.au/environment/pollution/monitoring/air/air-monitoring/measuring/aerosols#> (accessed Feb 19, 2020).
- ²⁵ Lockwood, D. J. Rayleigh and Mie scattering. *Encyclopedia of Color Science and Technology*, 1st ed.; Luo, M. R. ed.; Springer New York: New York, NY, 2016; pp. 1097-1107.

Chapter 3. Changes in Aerosol Optical Properties Induced by SOA Coating

In this section, I describe experiments to evaluate the changes of morphological and optical properties of soot particles as a result of an aging process induced by a p-xylene derived secondary organic aerosol (SOA) coating. The detailed sample preparation steps are described in Chapter 2. Fresh soot was generated by a McKenna burner and then passed through a dryer, a thermodenuder, and a counter-flow parallel-plate membrane denuder (CPMD) to remove water and volatile organics. Then I selected soot particles with a diameter of 250 nm using a differential mobility analyzer (DMA) and introduced those particles into the smog-chamber until a concentration of about 1000 particles/cm³ was reached. The soot concentration in the chamber was monitored using a condensation particle counter (CPC). P-xylene was used as SOA precursor and 0.5 ppm of p-xylene was added through a bubbler into the chamber. For the production of OH radicals, 0.5 ml of hydrogen peroxide (H₂O₂) was injected into the chamber by a syringe. The UV lights were switched on after the injection of H₂O₂ to generate OH radical and to initiate the photochemical reaction to form SOA which coats the soot particles.

In order to monitor the soot particle aging process, the measurements commenced after the UV lights were switched on. The measurement data collected are particle diameter, particle mass, scattering coefficient, and absorption coefficient. The soot sample was extracted from the smog chamber through tubing which was separated into two paths. One path led to a centrifugal particle mass analyzer (CPMA) followed by a CPC to determine particle mass and concentration. The sample in the second path was humidified before measuring the particle diameter, scattering coefficient, and absorption coefficient. I used a scanning mobility particle sizer (SMPS) to measure particle size and a photoacoustic extinctionsmeter (PAX) to measure scattering and absorption coefficients. Particle diameter, scattering coefficient, and absorption coefficient were also measured for particles with SOA coating removed with a

thermodenuder. Experiments were carried out under five different RH conditions (10%, 20%, 40%, 60%, and 70%), and for each RH I have done at least two to three runs. For the results I will show in the later sections, only one of the sets was used.

3.1. Soot Restructuring and Morphology Change

Previous studies have shown that soot aggregates collapse when coated with SOA.¹ This restructuring process is dependent on the source of the soot sample,² surface tension of the coating material,³ and the relative humidity (RH) of the surrounding environment.⁴

I determined the particle sizes from the SMPS data and plot them here as a function of measurement time. The SMPS can provide a particle size distribution within a scanning period of about 4 minutes. The peak of this distribution is taken as the average soot particle diameter during the scanning period. An SMPS measurement was done every 4 min after the UV lights were switched on. The total data collection time for all my experiments was initially 270 min and was later shortened to about 240 min. The results are shown below in Figure 3.1. The reason I shortened the experimental time was the introduction of three measurements in close succession, which resulted in a total sample outflow out of the smog chamber of 2.3 slpm. Since I did not refill the chamber with replacement air during the experiment, the smog chamber bag faced a risk of damage after long operation. This will be further discussed in Chapter 3.3.

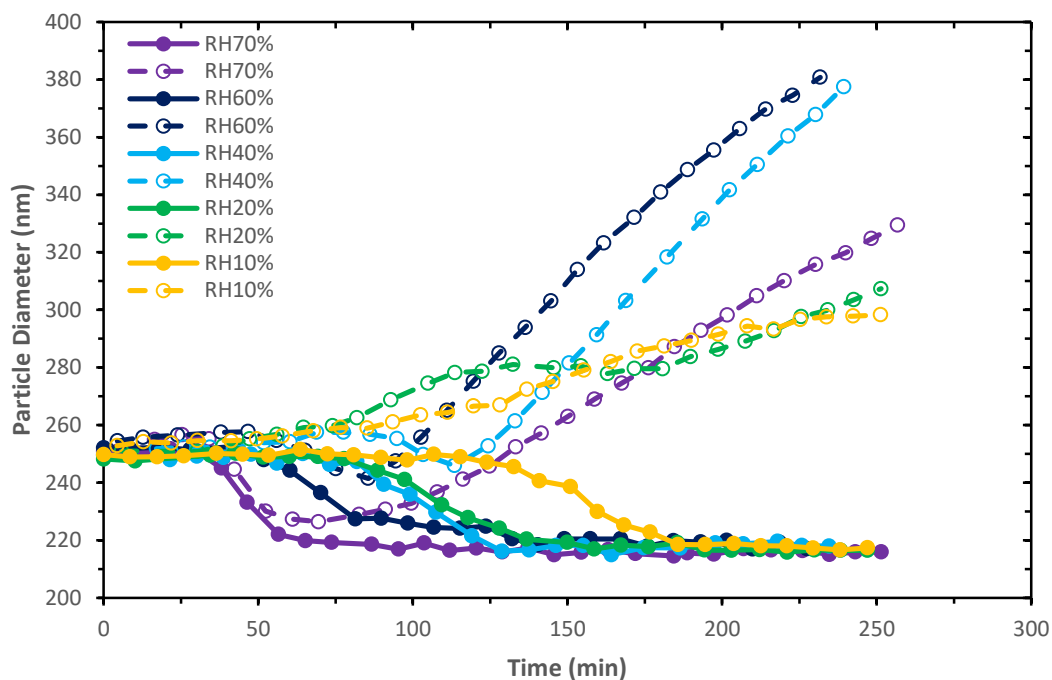


Figure 3.1. The change in particle diameter as function of reaction time for different relative humidities. (open circles: coated particles; solid circles: denuded particles)

I divide the graphs in Figure 3.1 into three categories (low RH, medium RH, and high RH) and discuss them in the following. One can see from the figure that the change in particle size during the experiment is dependent on the relative humidity. For low relative humidity (RH = 10%) there is a gradual increase in size of coated soot particles. The denuded particles experience three stages. There is essentially no change in particle size for the first two hours. The particle then undergoes a smooth decrease in size from 250 to about 220 nm, and then remains at this diameter for the rest of the experiment. This observation is somewhat different from a previous study by Leung et al., who deduced that low relative humidity (RH < 13%) leads to only little or no soot collapse.⁴ However, Leung et al. measured only the coated particle diameter and the collapse of the soot core is masked by the increasing SOA coating. The final particle size is also identical to those under higher RH conditions. When the RH increases to 20%, we can see four stages for coated particles and three stages for denuded particles during the experiment. At stage one, both coated and denuded

particle size stays at 250 nm for the first hour. Then, the coated particles start to grow, reaching about 280 nm in stage two. At the same time, the denuded particles start to collapse. The coated particles will come to stage three, where they reach a plateau for the following hour. At the end of this plateau, the coated particles move to stage four, where they begin to increase in size again. Meanwhile, the denuded particles move to stage three, where they reach the minimum size of 220 nm. When the RH exceeds 40%, the general trend for size changes is qualitatively similar. The denuded particles undergo three similar stages as for RH = 10% and 20%. However, for RH > 40%, the soot particles collapse earlier and faster. For coated particles, there are three stages, where stage one is similar as before having a constant size at 250 nm. Stage two starts simultaneously with the denuded particles, but with a smaller slope of size decrease and the coated particles reach the size minimum before the denuded particles. At stage three, no plateau is observed. Here, the soot particles grow rapidly throughout the remainder of the experiment.

In Figure 3.1, the increase in particle diameter for coated particles at 70% RH is slower than for 60% and 40% RH. The reason may be lower initial concentrations of p-xylene and H₂O₂, resulting in a slower SOA coating process.

A different method to present the result is to plot the diameter growth factor (Gfd) as function of mass growth factor (Gfm).¹ The mass/diameter growth factor can be calculated as the ratio of current particle mass/diameter to initial particle mass/diameter, as shown in Equations (3.1) and (3.2).¹

$$\text{Gfm} = \frac{m_{\text{particle}}}{m_{\text{soot}}} \quad (3.1)$$

$$\text{Gfd} = \frac{d_{\text{particle}}}{d_{\text{soot}}} \quad (3.2)$$

Here, m_{particle} is the current mass of the particle (including soot and SOA), m_{soot} is the initial mass of the soot particle, d_{particle} is the current mobility diameter of the particle (including soot and SOA), and d_{soot} is the initial mobility diameter of the soot particle.

The soot particle mass and its distribution were measured with a CPMA and a

CPC 3771. Coupling of CPMA and CPC can provide a mass distribution over a certain time period. The CPMA data can be analyzed to obtain, for example, an average soot particle mass, using a MATLAB program (CPMA_GUI_V2), which was provided to me by Kerry Chen from Dr. Olfert's group. This program plots the raw CPMA data which resemble a log-normal distribution and calculates the peak of this distribution. The peak can be considered as the average soot particle mass during the CPMA/CPC scanning period of about 4 minutes. Figure 3.2 shows the relationship between diameter growth factor and mass growth factor for coated particles, which indicates the increase in soot particle size change as an increasing amount of SOA condenses onto the soot particles. Here, I obtain similar information about the trends in particle diameter for RH from 10% to 70% as from Figure 3.1 (particle diameter vs. reaction time). For 10% RH, there is a continuous increase in diameter. For RH = 20%, there is a plateau located between $G_{fm} = 3$ and 5, while the remainder of the region shows an increasing trend of G_{fd} . For RH = 40, 60, and 70%, the trends are similar. I can observe three stages, similar to Figure 3.1. The local minimum for the G_{fd} shifts to smaller G_{fm} for higher RH values. In addition, higher RH values give rise to a larger slope for stage three.

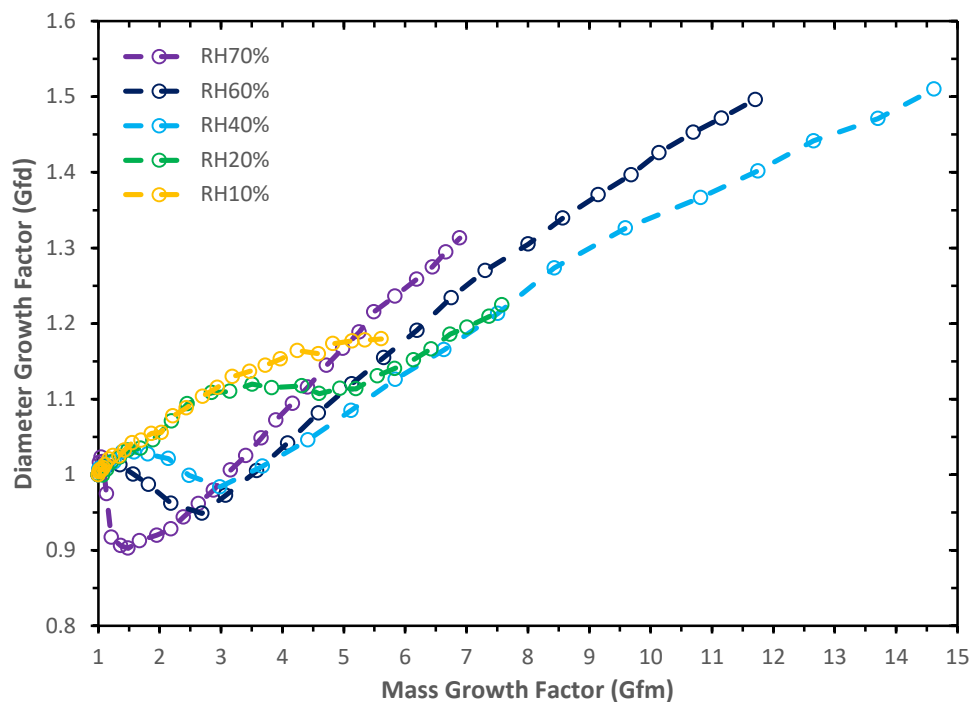


Figure 3.2. Diameter growth factor as function of mass growth factor at different relative humidities.

In general, my data agree quite well with previous measurements.⁴ The only exception is the trend for RH equals 20%. In the paper by Leung et al., the 20% RH trend is quite similar to those with higher RH.⁴ I believe this may be because of the different amounts of initial reactants and soot sample in both studies. In the studies by Schnitzler et al. and Leung et al., the morphological changes of soot particles were studied in terms of different SOA precursors and different relative humidity conditions. To produce SOA, precursor (such as p-xylene) concentrations of up to 2 ppm were used in the chamber and 1 ml H₂O₂ was injected.^{1,4} In my experiments, these amounts made the reaction proceed too rapidly to acquire meaningful data and I decreased the p-xylene concentration to 0.5 ppm and injected 0.5 mL H₂O₂. However, the SOA precursor, p-xylene, concentration is not easy to control and it is difficult to achieve the same concentration for each experiment. The early end point of the graphs for RH equals 20% and 70% in Figure 3.1 can be explained by a lower initial concentration of p-xylene.

From particle diameter and particle mass, I can calculate an effective density, ρ_{eff} , and shape factor, χ , defined in Equations (3.3) and (3.4).¹

$$\rho_{eff} = \frac{6m_{particle}}{\pi d_{particle}^3} \quad (3.3)$$

$$\chi = \frac{d_{particle} C_c(d_{ve})}{d_{ve} C_c(d_{particle})} \quad (3.4)$$

Here, $C_c(d_{particle})$ and $C_c(d_{ve})$ are Cunningham slip correction factors and d_{ve} is the volume equivalent diameter, which can be calculated using Equation (3.5).

$$d_{ve} = \left[\frac{6}{\pi} \left(\frac{m_{soot}}{\rho_{soot}} + \frac{m_{particle} - m_{soot}}{\rho_{SOA}} \right) \right]^{\frac{1}{3}} \quad (3.5)$$

Here, ρ_{soot} is the density of bare soot, $\rho_{soot} = 1.8 \text{ g/cm}^3$,⁴ and ρ_{SOA} is the density of SOA; the density of p-xylene derived SOA is 1.46 g/cm^3 .⁵

For $RH \geq 20\%$, the shape factor for coated soot particles decreases from 2.3 and converges to around 1.0, which indicates that the particle is almost spherical. In terms of denuded particles, the shape factor decreases from 2.3 and converges to around 1.8, which agrees with previous work where soot particle ageing was studied utilizing different SOA precursors.¹ The effective density of denuded particles increases from 0.35 g/cm^3 and converges to around 0.6 g/cm^3 , which indicates that the soot aggregates become more compact. This value also agrees with Dr. Schnitzler's work.¹ As for the coated particles, the effective density increases from 0.35 g/cm^3 and converges to values from around 1.2 to 1.5 g/cm^3 . One observation here is that the effective density of the coated particles at RH of 20% and 40% converge to around 1.5 g/cm^3 , which is close to p-xylene SOA density, 1.46 g/cm^3 . As RH increases from 40% to 70%, the converged effective density decreases, presumably because of uptake of water.

For $RH = 10\%$, due to insufficient experimental time, I do not see the coated particle lines converge to any of the two scenarios. Nevertheless, the decreasing trend for shape factor and the increasing trend for effective density are observed.

3.2. Measurements of Absorption and Scattering Coefficients

In this section, I describe my measurements of absorption, B_{abs} , and scattering

coefficients, B_{sca} , of the soot particles using a photoacoustic extinctions (PAX). The PAX can provide data for these coefficients at a rate of 1 Hz. First, I need to find out the correct sampling time interval that aligns with the SMPS and CPMA scans. The actual PAX measurement time to collect data is 170 seconds and I set the sampling time interval to 240 seconds. This allows me to obtain the particle mass, diameter, scattering coefficient, and absorption coefficient all at the same time.

3.2.1. Scattering

3.2.1.1 Scattering Coefficient

For each PAX measurement cycle there are 170 individual measurements, corresponding to one scattering coefficient value for each second. The average of the 170 scattering coefficients is calculated for each cycle and is plotted as function of time in Figure 3.3 and Figure 3.4 for coated and denuded soot particles, respectively. The error bars in the figures indicate the standard deviation from the 170 individual measurements in each measurement cycle.

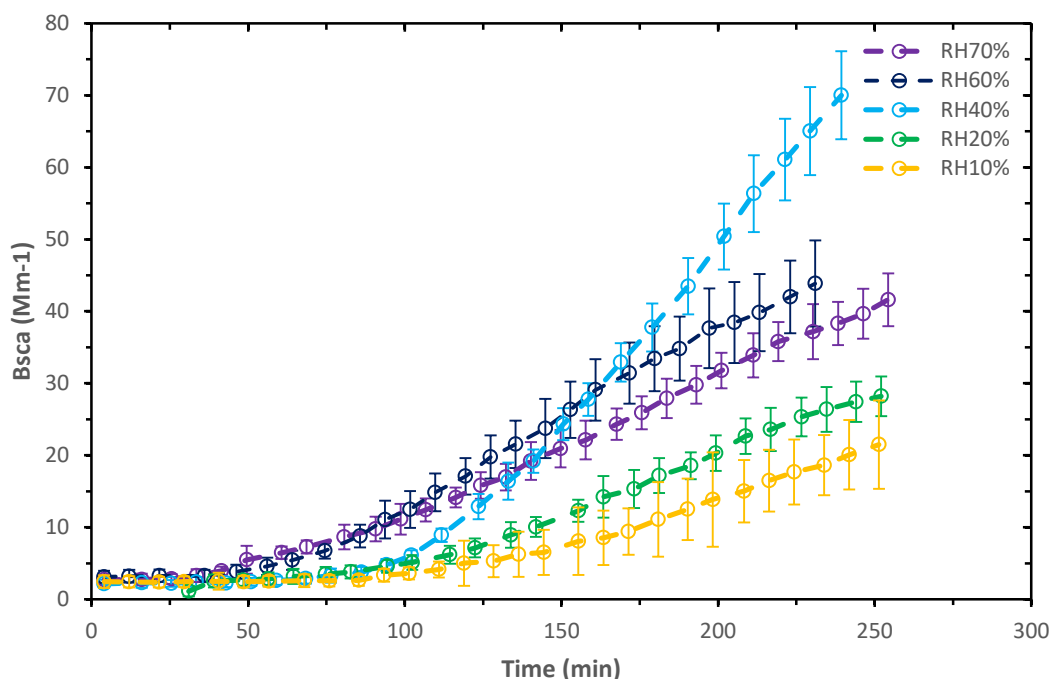


Figure 3.3. Average scattering coefficient of coated soot particles as function of reaction time for different relative humidities.

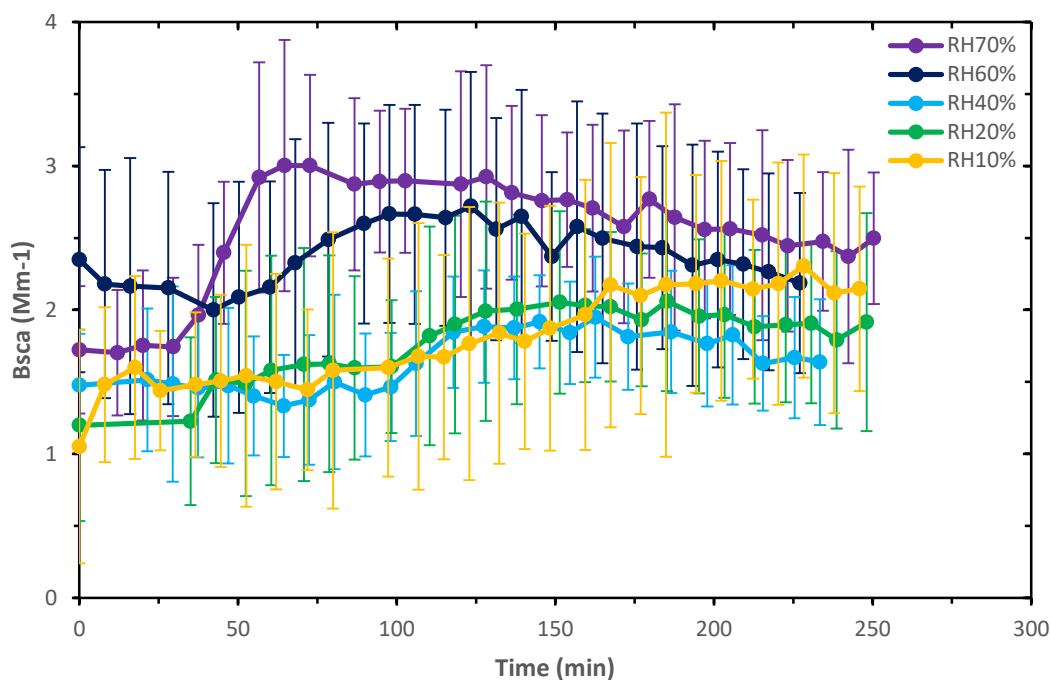


Figure 3.4. Average scattering coefficient of denuded soot particles as function of reaction time for different relative humidities.

The scattering coefficient for coated particles shows an increasing trend in Figure 3.3, which is a result of the increasing SOA coating.⁶ To confirm this, I have done a background experiment with p-xylene derived SOA particles without soot core. In this experiment, I skipped the soot preparation part and began with admitting p-xylene and H₂O₂ into the chamber. Since I needed to grow SOA particles of similar size to the original soot sample, I provided relatively large amounts of both reactants: p-xylene with a concentration of 2.5 ppm and 5 ml of H₂O₂. During the experiment, the formed SOA particles were analyzed by SMPS and PAX. After 20 min UV light exposure, I first confirmed that p-xylene SOA particles were generated with an average diameter of 71 nm. This point in time was set as time = 0. The corresponding average scattering coefficient is 5.3 Mm⁻¹. A plot of the resulting data is shown in Figure 3.5. It can be seen that the scattering coefficient increases exponentially as function of time. This is what I am expected because in Figure 3.3, the scattering coefficient for coated soot particles at all RH conditions show rapidly increasing trends. The increase is a result

of the growth of the particles.

According to my measurements, the SOA particle concentration shows a logarithmic increasing trend, and reaches a plateau at around 15000 particles/cm³ after 40 minutes of UV exposure. The SOA particle diameter at that time is around 170 nm. It takes about another 20 minutes for the SOA particle diameter to reach a value of about 290 nm. The average scattering coefficient at this point is about 640 Mm⁻¹. From these data, it is clear that it is the SOA coating that gives rise to the increasing scattering coefficient as the soot particles age. The reason I do not include the absorption coefficient data is because the absorption coefficient does not change with time. Compared to scattering coefficients, the values of the absorption coefficients are very small throughout the experiment, at around 2 Mm⁻¹.

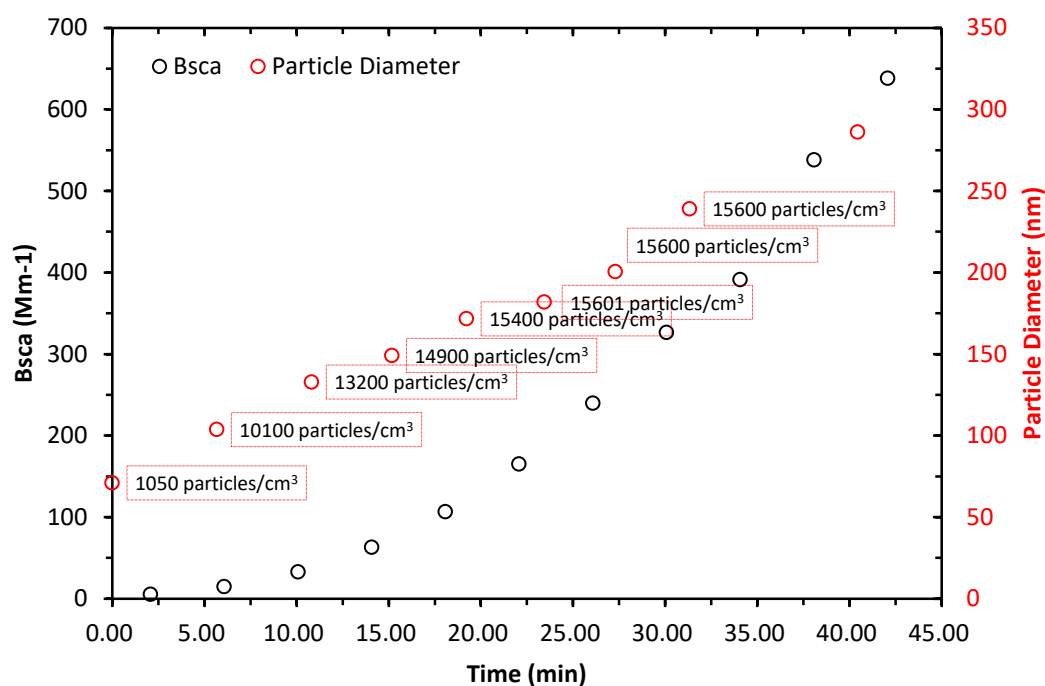


Figure 3.5. Scattering coefficient, particle diameter, and concentration as function of reaction time of p-xylene derived SOA.

What is interesting in comparing Figures 3.3 and 3.1 is that the time when the soot particle diameter begins to decrease at the end of their first stage is also the time when the scattering coefficients of the coated soot particles start to show an increasing

trend. The stages in the RH = 10% data are not so distinguishable and the trend is more or less monotonically increasing in Figure 3.1. However, for RH \geq 20%, the soot particle diameter changes are not monotone. There is either a plateau or a local minimum in the data, but these symptoms are not observable in Figure 3.3, where the scattering coefficients of the coated particles are plotted.

For denuded particles with RH \geq 20%, I can see three stages in Figure 3.4. In stage one from 0 to 50 min, the scattering coefficients are relatively stable, and this corresponds to the same time period in Figure 3.1, where the soot particle size is stable. When soot particles start to collapse, the scattering coefficient increases. The time at which the maximum scattering coefficient is reached is very close to the time where the soot particle size has decreased to its minimum (for example at RH = 70%, the time is around 65 min). The time for stage two is not identical between Figures 3.4 and 3.1 because a higher RH leads to faster collapse, which results in a shorter time period. In Figure 3.4, the scattering coefficients for RH \geq 20% show decreasing trends in stage three (for example at RH = 70% in stage three, i.e. the time period from 65 to 250 min, the scattering coefficient drops from 3.0 to 2.5 Mm^{-1}), which is a result of the loss of soot particles,⁷ which is mainly due to wall effects.^{8,9} For the plot with RH = 10% in Figure 3.4, these three stages are not so distinguishable, but one can still see a clear increase from about 1.6 Mm^{-1} at 100 minutes to around 2.2 Mm^{-1} at 170 minutes. This time range is similar to stage two in Figure 3.1 (time from around 100 to 190 minutes).

3.2.1.2. Mass Scattering Cross-section

To remove the influence of the decrease in sample concentration during the experiment, I have calculated the mass scattering cross-section (MSC), which is given by Equation (3.6).¹⁰

$$\text{MSC} = \frac{B_{\text{sca}}}{[\text{particle}] \times m_{\text{particle}}} \quad (3.6)$$

Here, $[\text{particle}]$ is the particle number concentration (the particle here includes soot

and SOA coating) and B_{sca} is the scattering coefficient.

The trend of the MSC as function of time is shown below in Figure 3.6 and Figure 3.7. I discuss the denuded particles (Figure 3.6) first. I can still observe three stages for these curves, similar to the scattering coefficients shown in Figure 3.4. However, for stage three, the decreasing trend is replaced by a plateau (for example at RH = 70%, stage three is from 65 to 250 min). This result is reasonable because at this final stage, the morphology of the soot particle remains the same.

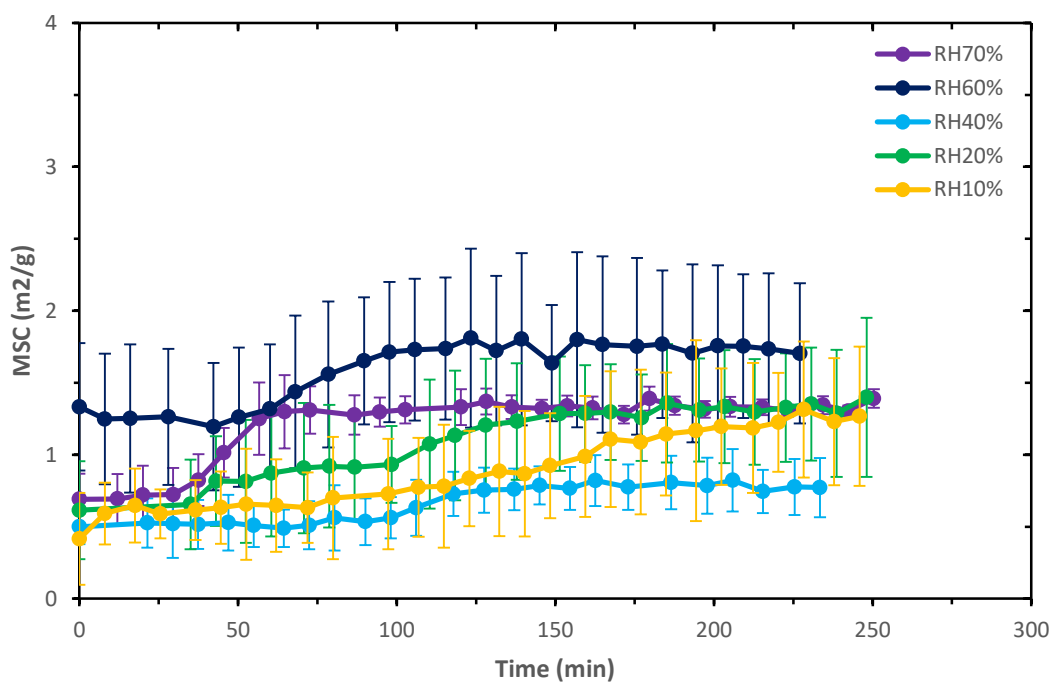


Figure 3.6. Mass scattering coefficient of denuded soot particles as function of time for different relative humidities.

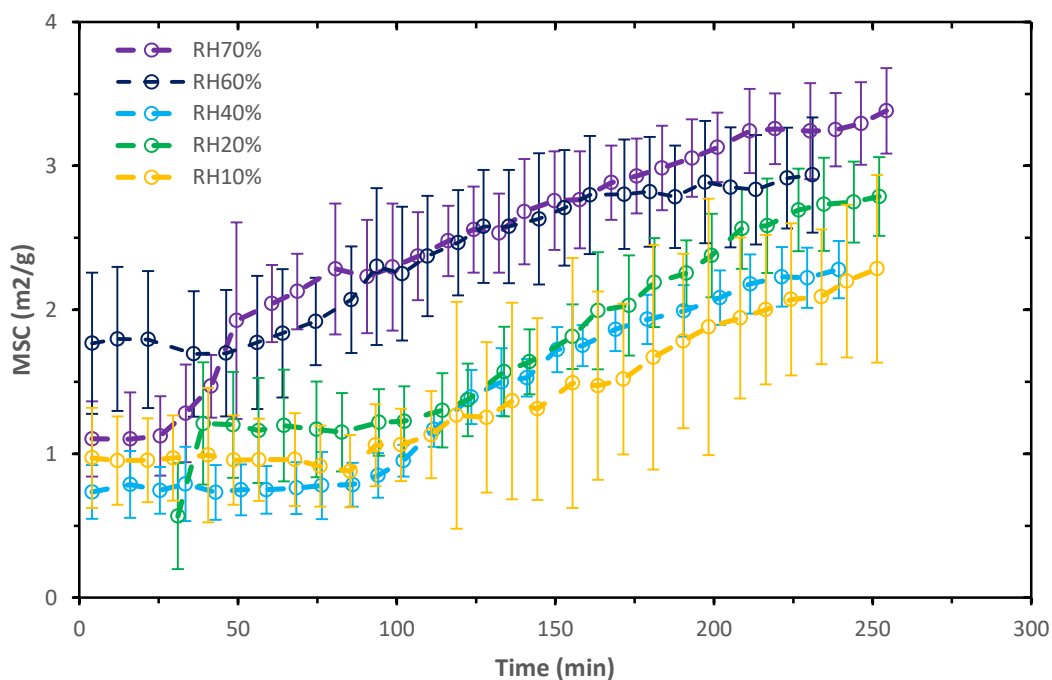


Figure 3.7. Mass scattering coefficient of coated soot particles as function of time for different relative humidities.

In Figure 3.6, particles at $RH = 40\%$ have the lowest MSC values in all three stages. A low RH condition means that the SOA coating is very viscous, while high RH conditions mean that the SOA coating has a larger surface tension compared to low RH.⁴ In the intermediate region of $RH = 40\%$, the SOA coating is not very viscous but can still induce a significant soot aggregate restructuring.

For $RH=60\%$ the initial MSC values are much larger than those for the other relative humidities. A somewhat similar trend can be seen in Figure 3.4 for the average scattering coefficients. It looks to me that this curve is somehow shifted upward by about $1 \text{ m}^2/\text{g}$. This could be the result of a systematic error on that measurement day. The PAX is very sensitive to black carbon sample, and my initial sample concentration was merely around $1000 \text{ particles}/\text{cm}^3$, which is quite small. Another possibility is that there might have been some soot contaminating the reciprocal nephelometer, because I do not see a significant shift in the absorption coefficient measurements.

In terms of the coated particles in Figure 3.7, the MSC values are generally increasing with time, with two stages visible throughout all RH conditions. The overall trends of the curves are quite similar. This is what is expected, because the particle size increases due to the SOA coating. In stage one, the MSC shows an almost horizontal trend. When moving to stage two ($RH \leq 40\%$ at about 80 min $RH \geq 60\%$ at about 30 min), the MSC starts to increase. What is interesting here is that for $RH \leq 20\%$, the shape of the curves are concave up, while for $RH \geq 60\%$, the shapes are concave down (stage two only). The curve for $RH = 40\%$ shows a concave up shape for the first 130 min, and then tends towards a concave down shape. A concave up shape indicates an increasing slope and the initial slope is small, while a concave down shape indicates a decreasing slope and the initial slope is large (see Figure 3.7 between about 0-130 and 130-250 min). As I have mentioned in Chapter 2, I used nearly the same amount of SOA precursors p-xylene and H_2O_2 for each experiment. It would be very valuable to extend the experiment time and to monitor if the final MSCs will eventually converge for different RH conditions. If that were the case, high RH would merely increase the rate of the coating process.

3.2.2. Absorption

3.2.2.1. Absorption Coefficient

The average absorption coefficients for both coated and denuded soot particles are plotted as a function of reaction time in Figure 3.8 and 3.9 for different relative humidities.

Unfortunately, I cannot see a clear particle size dependence of the absorption coefficient for either coated or denuded soot particles. What is clear here is that p-xylene derived SOA coating gives rise to an absorption enhancement.¹¹ Wall effects may also play a role here, because all curves show slightly decreasing trends. What is interesting here is that soot restructuring does not seem to affect the absorption coefficient. Also, an increase in mass of SOA coating does not influence the absorption coefficients significantly.

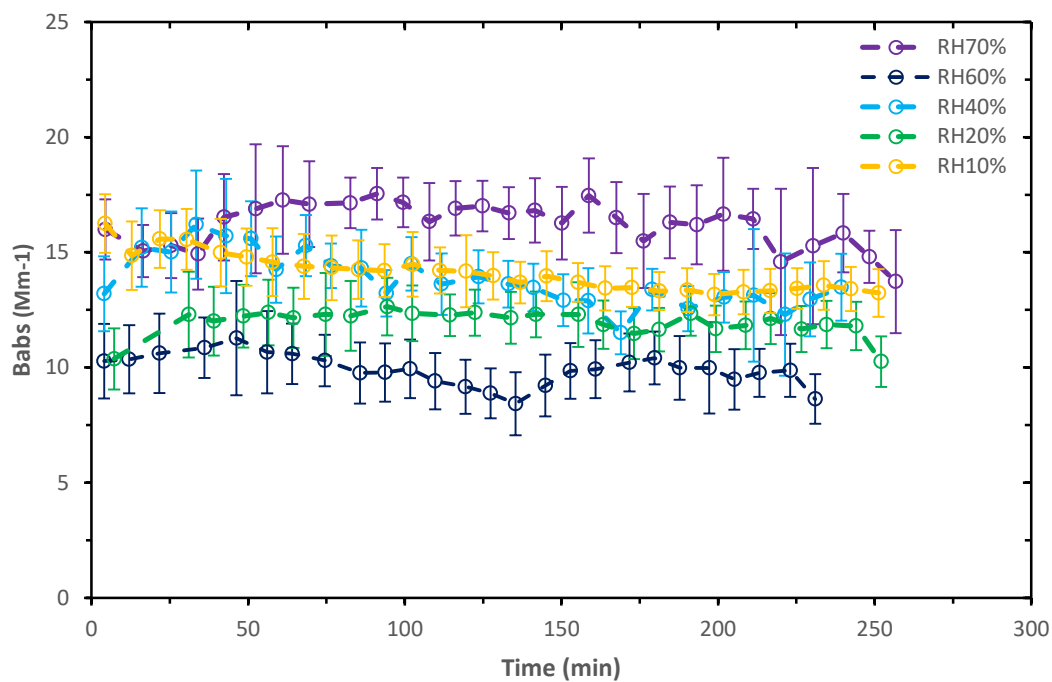


Figure 3.8. Absorption coefficient of coated soot particles as function of reaction time for different relative humidities.

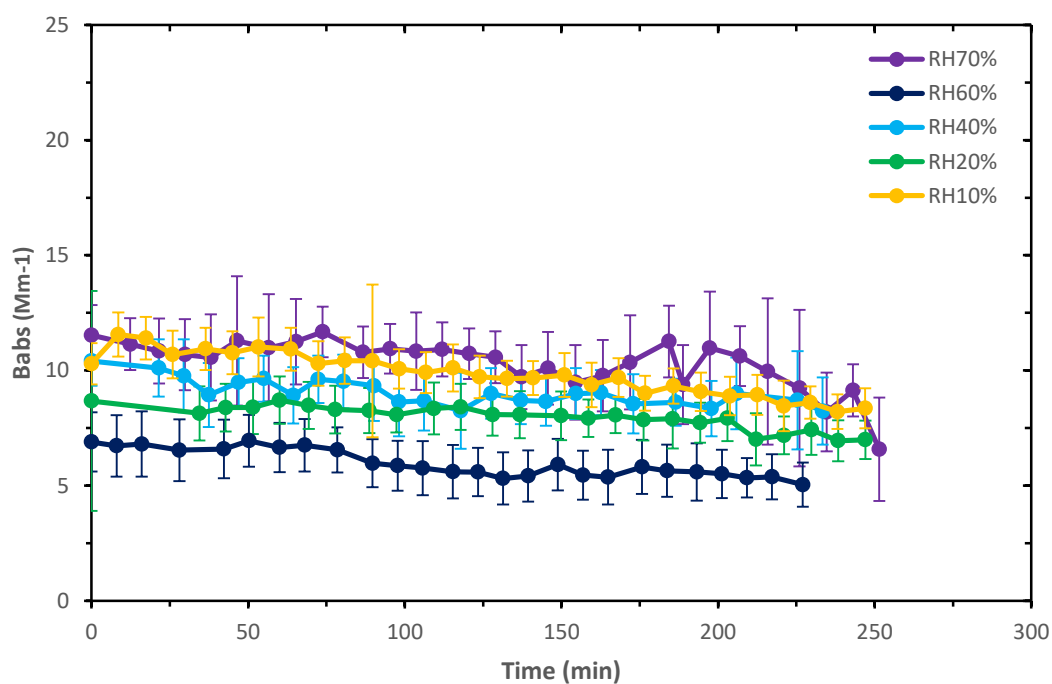


Figure 3.9. Absorption coefficient of denuded soot particles as function of reaction time for different relative humidities.

3.2.2.2. Mass Absorption Cross-section

Similar to the case of the mass scattering cross section, a mass absorption cross-section (MAC) can be defined by Equation (3.7) to obtain the absorption cross-section per mass unit.¹⁰

$$\text{MAC} = \frac{B_{abs}}{[particle] \times m_{particle}} \quad (3.7)$$

Here, B_{abs} is absorption coefficient, $[particle]$ the particle number concentration, and $m_{particle}$ is the particle mass.

The trend of MAC as a function of reaction time is shown below in Figure 3.10. Similar to the observations for the MSC, particles under low RH ($\leq 20\%$) and high RH (70%) conditions tend to have greater MACs than those in the intermediate range (RH=40% and 60%). This result is similar to findings in a previous study by Khalizov et al,¹² where they found that bare soot particle have lowest MACs in intermediate RH conditions (RH = 50%).

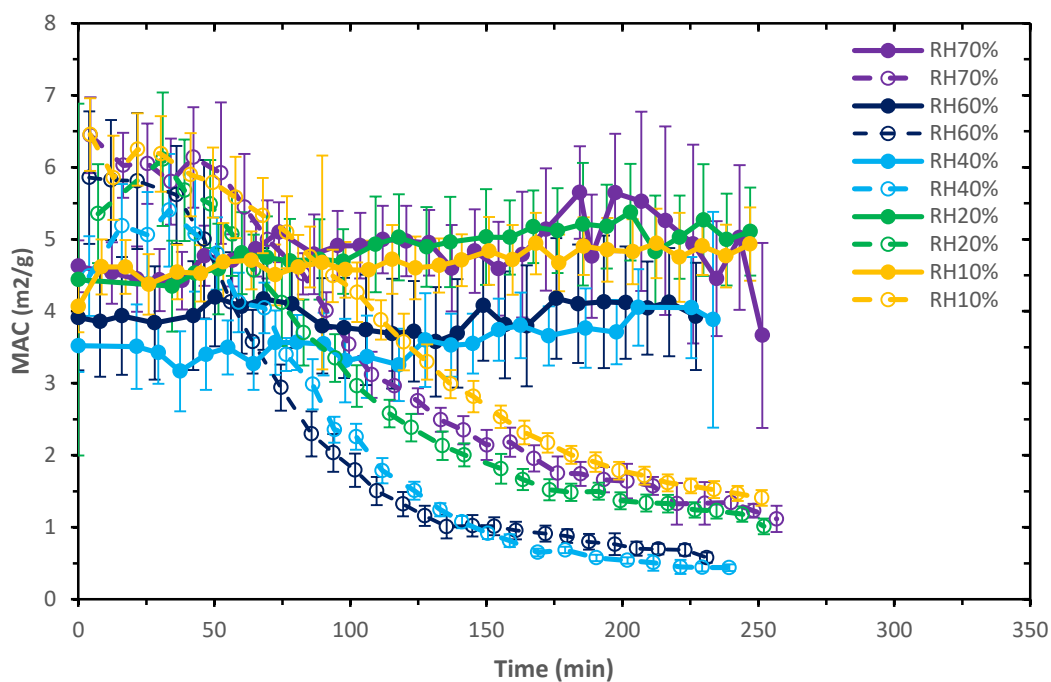


Figure 3.10. Mass absorption coefficient as function of reaction time at different relative humidities. (Hollow symbols: coated particles; solid symbols: denuded particles)

For denuded particles, there is an only slightly increasing trend of MAC with reaction time for all RH condition, which means that the MAC does not change much due to soot particle restructuring. On the other hand, for coated soot particles two stages are noticeable for the MAC for all RH conditions. In the first stage, a flat or slight increasing trend is observed for the first 30-40 minutes. This is because p-xylene derived SOA has not yet condensed onto the particle to a significant degree and the mass of “coated” soot particle is still close to that of the bare soot particle. In the second stage, the MAC undergoes a rapid decrease, which is a result of the fast increase in particle mass.

To reduce the risk of condensing water inside the CPMA, I have connected the CPMA to my sample line before visiting the humidifier. This means that I have never measured the mass of water, so the MAC I have calculated will be slightly too large. Although κ -Köhler theory can be used to calculate the mass of water at specific Gfm,⁴ it is difficult to apply in my case. The reason is because the Gfm end points of the curves in Figure 3.2 for different RH conditions are quite distinct. Under dry conditions (RH equals 10% and 20%), the particle mass can only grow by a factor of around 6 to 7, while for RH equals 60% and 70%, the particle mass can increase by a factor of more than 10.

3.2.2.3. Mass Absorption Cross-section with Respect to Mass of Bare Soot Particles

In order to remove the effects from the rapid increase of SOA coating mass, I decided to calculate the MAC with respect to bare soot particles by Equation (3.8).

$$MAC(bare\ soot) = \frac{B_{abs}}{[particle] \times m_{soot}} \quad (3.8)$$

Here, I replaced $m_{particle}$ in Equation 3.7 with m_{soot} . The m_{soot} is measured at the very beginning of the experiment, so that MAC(bare soot) represents the absorption coefficient per mass concentration of soot.

The trend of MAC(bare soot) as a function of Gfm is shown in Figure 3.11. I

plotted MAC(bare soot) as a function of Gfm because I want to illustrate the relationship between absorption enhancement and increase in the amount of SOA coating. For this purpose, the Gfm is a better option as the independent variable than coating mass because the Gfm is not affected by the slightly different amounts of p-xylene for each experiment. At low RH ($\leq 20\%$) and high RH (70%) the MAC(bare soot) increases from Gfm between 0 and 5. From Gfm equals 5 to 7, it is hard to identify whether these curves are still increasing or reach a plateau. The reason why there are larger final mass growth factors at RH 40% and 60% is probably because of a larger initial amount of p-xylene. Interestingly, at RH of 40% and 60%, the MAC(bare soot) increases only very slightly. In addition, at intermediate RH conditions the MAC(bare soot) values are lower compared to low and high RH conditions. This result is also similar to the study done by Khalizov et al,¹² where they found that particles at RH=50% gives a local minimum of the MAC for soot particles mixed with sulfuric acid.

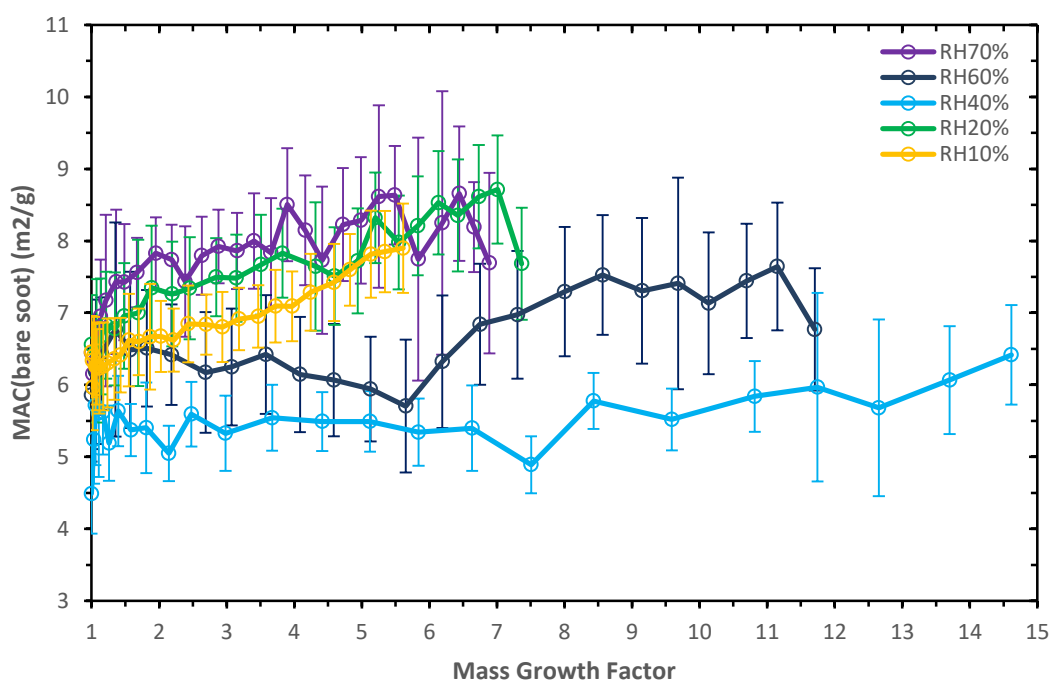


Figure 3.11. Mass absorption coefficient with respect to the mass of the bare soot particles as function of mass growth factor for different relative humidities.

3.3. Error Discussion

In this section, I point out potential errors in the data collection and some future improvements.

It can be noticed that the initial readings of scattering coefficients for all RH conditions are quite low and they vary. As shown in Figure 3.4 for example, the initial scattering coefficients vary between 1.1 to 2.3 Mm^{-1} . Also, the error bars, particularly in scattering measurements for denuded particles, are relatively large, which is a consequence of the low values for the denuded particle scattering coefficients. The average standard deviation of the denuded particle scattering coefficients is about 0.7 Mm^{-1} . This is quite a large error compared to the data. For $\text{RH} \leq 40\%$ in stage one, the scattering coefficients are within the range of 1.1 to 1.5 Mm^{-1} . One reason is because the initial soot particle concentration may be slightly different between each experiment. As I have introduced in Chapter 2, I need to prepare about 1000 particles/ cm^3 soot sample inside the smog chamber. The fluctuation here is about 10 to 20%. As I have mentioned before, the soot sample concentration is low. This is due to the long filtering as well as the size selection process. For example, passing through an operating DMA will reduce the soot concentration by about a factor of 100. One improvement I can think of is to upgrade the soot generation source or clean the McKenna burner once we notice a production decay.

Another issue is the limited measurement time. Our perfluoroalkoyl (PFA) bag is located in the center of the aluminum housing and is suspended in the housing at four of its edges. As a result, the bag cannot be deflated too much to avoid a tear. In some of the experiments described in this thesis a PAX, CPMA, CPC 3771, and CPC 3776 are used as detectors, which leads to a total sample outflow of 2.3 slpm. During an experiment time of 270 minutes a total of 621 L sample is extracted, which is about one-third of the volume of the PFA bag. This is the reason why I considered 270 minutes as my limiting experiment time. To increase this experiment time, one could add valves before these characterization instruments and only use sample flow during the actual measurement. However, this may cause some fluctuations especially for the

RH dependence studies.

References

- ¹ Schnitzler, E. G.; Dutt, A.; Charbonneau, A. M.; Olfert, J. S.; Jäger, W. Soot aggregate restructuring due to coatings of secondary organic aerosol derived from aromatic precursors. *Environ. Sci. Technol.* **2014**, *48*, 14309-14316.
- ² Leung, K. K.; Schnitzler, E. G.; Dastanpour, R.; Rogak, S. N.; Jäger, W.; Olfert, J. S. Relationship between coating-induced soot aggregate restructuring and primary particle number. *Environ. Sci. Technol.* **2017**, *51*, 8376-8383.
- ³ Schnitzler, E. G.; Gac, J. M.; Jäger, W. Coating surface tension dependence of soot aggregate restructuring. *J. Aerosol Sci.* **2017**, *106*, 43-55.
- ⁴ Leung, K. K.; Schnitzler, E. G.; Jäger, W.; Olfert, J. S. Relative humidity dependence of soot aggregate restructuring induced by secondary organic aerosol: effects of water on coating viscosity and surface tension. *Environ. Sci. Technol. Lett.* **2017**, *4*, 386-390.
- ⁵ Nakao, S.; Tang, P.; Tang, X.; Clark, C. H.; Qi, L.; Seo, E.; Asa-Awuku, A.; Cocker III, D. Density and elemental ratios of secondary organic aerosol: Application of a density predication method. *Atmos. Environ.* **2013**, *68*, 273-277.
- ⁶ Saathoff, H.; Naumann, K.-H.; Schnaiter, M.; Schöck, W.; Möhler, O.; Schurath, U.; Weingartner, E.; Gysel, M.; Baltensperger, U. Coating of Soot and (NH₄)₂SO₄ particles by ozonolysis products of α -pinene. *J. Aerosol Sci.* **2003**, *34*, 1297-1321.
- ⁷ Redmond, H.; Thompson, J. E. Evaluation of a quantitative structure-property relationship (QSPR) for predicting mid-visible refractive index of secondary organic aerosol (SOA). *Phys. Chem. Chem. Phys.* **2011**, *13*, 6872-6882.
- ⁸ McMurry, P. H.; Grosjean, D. Gas and aerosol wall losses in Teflon film smog chamber. *Environ. Sci. Technol.* **1985**, *19*, 1176-1182.
- ⁹ Miracolo, M. A.; Hennigan, C. J.; Ranjan, M.; Nguyen, N. T.; Gordon, T. D.; Lipsky, E. M.; Presto, A. A.; Donahue, N. M.; Robinson, A. L. Secondary aerosol formation from photochemical aging of aircraft exhaust in a smog chamber. *Atmos. Chem. Phys.* **2011**, *11*, 4135-4147.

-
- ¹⁰ Xue, H.; Khalizov, A. F.; Wang, L.; Zheng, J.; Zhang, R. Effects of dicarboxylic acid coating on the optical properties of soot. *Phys. Chem. Chem. Phys.* **2009**, *11*, 7869-7875.
- ¹¹ Schnaiter, M.; Linke, C.; Möhler, K.-H. N.; Saathoff, H.; Wagner, R.; Schurath, U. Absorption amplification of black carbon internally mixed with secondary organic aerosol. *J. Geophys. Res.* **2005**, *110*, D19204.
- ¹² Khalizov, A. F.; Xue, H.; Wang, L.; Zheng, J.; Zhang, R. Enhanced light absorption and scattering by carbon soot aerosol internally mixed with sulfuric acid. *J. Phys. Chem.* **2009**, *113*, 1066-1074.

Chapter 4. Conclusions

Based on my current results, the scattering coefficient, B_{sca} , of coated soot particles increases with growing overall particle size by a factor from 8.8 to 32.4, depending on the RH. Soot particle restructuring can also induce a small increase in B_{sca} by a factor of about 1.5. The same trend can be seen for the MSC, which increases by a factor of 2.54 for size increase through coating and by a factor of 1.66 during particle collapse. B_{sca} and MSC increase with growing particle size because the soot particles fall within the Mie scattering regime,¹ where scattering increases with particle size.² What is interesting here is that the collapse of the soot particles due to restructuring also leads to an increase in scattering. This is probably due to the increase in effective density of the particle. The soot restructuring process leads to a decrease of the mobility diameter of the denuded particles and the gap between the primary particles within the soot particle gets smaller. This may increase the chance of light hitting the soot, which then increases the scattering. The MSC at low and high RH have greater values than for RH =40%.

The absorption coefficient, B_{abs} , increases initially up to a growth factor of about 1.5 simply because of the presence of the SOA coating. However, B_{abs} is not affected by soot restructuring or an increasing SOA coating mass. This means that soot particles with SOA coating have larger B_{abs} compared to bare soot, but B_{abs} for soot with different mass of SOA coating will not change. Also, the change of size in soot particle will not influence B_{abs} . The mass absorption coefficient, MAC, for the denuded particles increases by a factor of only about 1.1 during the restructuring process. For coated particles, the MAC value decreases exponentially, since B_{abs} remains almost constant and the mass of the SOA coating grows quite fast. Here, I have observed a trend similar to the scattering coefficient. At intermediate RH (40% and 60%) lower values of the MAC are observed. At low RH (10% and 20%) and high RH (70%) circumstances, the MAC for both coated and denuded particle are very close. In terms of MAC(bare soot), I can easily distinguish that RH=40% gives

the lowest values. At low RH (10% and 20%) and high RH (70%) circumstances, MAC(bare soot) values are close to each other and RH=60% is an intermediate case.

In summary, RH=40% (medium RH) gives rise to low absorption. This is probably because at intermediate RH conditions, the SOA coating is not very viscous and the soot restructuring process is not very fast. This means that the viscosity and the speed of restructuring process are moderate, thus providing enough time for the SOA to fill the inside pores of the soot particles. At low RH, the SOA coating may be too viscous to fill in the pores. At high RH, the soot restructuring process is fast. According to Khalizov et al,³ low concentration of sulfuric acid coating tends to show lower MAC. So I am proposing that the SOA coating at intermediate RH can induce a dilution of SOA. Future studies are required to prove this.

What is also interesting about the trend of the absorption coefficients is that they do not change much due to soot restructuring or increase in SOA mass. This can be summarized as absorption not being dependent on particle size change. Absorption enhances with the coating of SOA, but the amount of SOA does not seem to matter. I think this is because we can consider soot plus SOA coating as whole material or a medium. So the refractive index of this medium is relatively stable. The size or the mass of this material will not affect the refractive index. Only the component of the SOA will affect the refractive index.

In my thesis, I have shown that for bare soot particles, absorption coefficients are larger than scattering coefficients, meaning that the absorption for bare soot particles is more significant than scattering. However in the real atmosphere, the soot particles are usually coated. The current study shows that the optical properties of the coated particles is strongly dependent on the SOA coating and the particular RH. It would be interesting to see in future work that how the morphological and optical properties change under varying RH conditions. For example, one could monitor the changes under an increasing or decreasing RH. I hope that my study contributes to a better understanding of the effect of soot particles on the global climate.

References

- ¹ Lockwood, D. J. Rayleigh and Mie scattering. *Encyclopedia of Color Science and Technology*, 1st ed.; Luo, M. R., ed.; Springer New York: New York, NY, 2016; pp. 1097-1107.
- ² McDonlad, J. E. Visibility reduction due to jet-exhaust carbon particles. *J. Appl. Meteorol.* **1962**, 1, 391-398.
- ³ Khalizov, A. F.; Xue, H.; Wang, L.; Zheng, J.; Zhang, R. Enhanced light absorption and scattering by carbon soot aerosol internally mixed with sulfuric acid. *J. Phys. Chem.* **2009**, 113, 1066-1074.

Bibliography

- Atkinson, R.; Arey, J. Atmospheric degradation of volatile organic compounds. *Chem. Rev.* **2003**, *103*, 4605-4638.
- Bohren, C. F.; Huffman, D. R. Absorption and scattering by a sphere. *Absorption and Scattering of Light by Small Particles*. Wiley: New York, 1998; pp. 83-129.
- Bond, T. C.; Sun, H. Can reducing black carbon emissions counteract global warming? *Environ. Sci. Technol.* **2005**, *39*, 5921-5926.
- Boucher, O.; Randall, D.; Artaxo, P.; Bretherton, C.; Feingold, G.; Froster, P.; Kerminen, V.-M.; Kondo, Y.; Liao, H.; Lohmann, U.; Rasch, P.; Satheesh, S. K.; Sherwood, S.; Stevens, B.; Zhang, X. Y. Clouds and aerosols. In *Climate Change 2013: The Physical Science Basis. Contribution of Working Group I to the Fifth Assessment Report of the Intergovernmental Panel on Climate Change*; Stocker, T.F.; Qin, D.; Plattner, G.-K.; Tignor, M. M.; Allen, S. K.; Boschung, J.; Nauels, A.; Xia, Y.; Bex, V.; Midgley, P. M., Eds.; Cambridge University Press: Cambridge, 2013; pp. 571-657.
- Burners. <http://www.flatflame.com/burner-description.html> (accessed Feb 19, 2020).
- Cox, A.J.; DeWeerd, A. J.; Linden, J. An experiment to measure Mie and Rayleigh total scattering cross section. *Am. J. Phys.* **2002**, *70*, 620-625.
- Després, V.; Huffman, J. A.; Burrows, S. M.; Hoose, C.; Safatov, A.; Buryak, G.; Fröhlich-Nowoisky, J.; Elbert, W.; Andreae, M.; Pöschl, U.; Jaenicke, R. Primary biological aerosol particles in the atmosphere: a review. *Tellus B: Chemical and Physical Meteorology*. **2012**, *64:1*, 15598.
- Droplet Measurement Technologies. Photoacoustic extinciometer operator manual. **2014**.
- Grainger, R. G.; Lucas, J.; Thomas, G. E.; Ewen, G. B. L. Calculation of Mie derivatives. *Appl. Opt.* **2004**, *43*, 5386-5393.
- Gao, G.; Jang, Myoseon. Effects of particle acidity and UV light on secondary organic aerosol formation from oxidation of aromatics in the absence of NO_x. *Atmos. Environ.* **2007**, *41*, 7603-7613.

- Guo, S.; Hu, M.; Lin, Y.; Gomez-Hernandez, M.; Zamora, M. L.; Peng, J.; Collins, D. R.; Zhang, R. OH-Initiated oxidation of m-xylene on black carbon aging. *Environ. Sci. Technol.* **2016**, *50*, 8605-8612.
- Healy, R. M.; Temime, B.; Kuprovskyte, K.; Wenger, J. C. Effect of relative humidity on gas/particle partitioning and aerosol mass yield in the photooxidation of p-xylene. *Environ. Sci. Technol.* **2009**, *43*, 1884-1889.
- Hinds, W. C. Introduction. *Aerosol Technology Properties, Behavior, and Measurement of Airborne Particles*, 2nd ed.; Wiley: New York, 1999; pp. 1-14.
- Hinds, W. C. Optical Properties. *Aerosol Technology Properties, Behavior, and Measurement of Airborne Particles*, 2nd ed.; Wiley: New York, 1999; pp. 349-378.
- Hu, Z. Spatial analysis of MODIS aerosol optical depth, PM_{2.5}, and chronic coronary heart disease. *Int. J. Health Geogr.* **2009**, *8*, 27.
- Hua, J.; Yin, Y.; Peng, L.; Du, L.; Geng,; Zhu. L. Acute effects of black carbon and PM_{2.5} on children asthma admissions: a time-series study in a Chinese city. *Sci. Total Environ.* **2014**, *481*, 433-438.
- Huang, M.; Zhang, W.; Hao, L.; Wang, Z.; Zhao, W.; Gu, X.; Fang, L. Low-molecular weight and oligomeric components in secondary organic aerosol from the photooxidation of p-xylene. *J. Chin. Chem. Soc.* **2008**, *55*, 456-463.
- Ismail, A. F.; Khulbe, K. C.; Matsuura, T. RO membrane characterization. *Reverse Osmosis*. Elsevier Inc., 2019; pp. 57-90.
- Jacobson, M. Z. Control of fossil-fuel particulate black carbon and organic matter, possibly the most effective method of slowing global warming. *J. Geophys. Res.* **2002**, *107*, 4410.
- Janssen, N. A. H.; Gerlofs-Nijland, M. E.; Lanki, T.; Salonen, R. O.; Cassee, F.; Hoek, G.; Fischer, P.; Brunekreef, B.; Krzyzanowski, M. Health effects of black carbon. World Health Organization: Copenhagen, Denmark, 2012.
- Khalizov, A. F.; Xue, H.; Wang, L.; Zheng, J.; Zhang, R. Enhanced light absorption and scattering by carbon soot aerosol internally mixed with sulfuric acid. *J.*

- Phys. Chem. A.* **2009**, *113*, 1066-1074.
- Kuwata, M. Particle classification by the tandem differential mobility analyzer-particle mass analyzer system. *Aerosol Sci. Technol.* **2015**, *49*, 508-520.
- Leung, K. K.; Schnitzler, E. G.; Dastanpour, R.; Rogak, S. N.; Jäger, W.; Olfert, J. S. Relationship between coating-induced soot aggregate restructuring and primary particle number. *Environ. Sci. Technol.* **2017**, *51*, 8376-8383.
- Leung, K. K.; Schnitzler, E. G.; Jäger, W.; Olfert, J. S. Relative humidity dependence of soot aggregate restructuring induced by secondary organic aerosol: effects of water on coating viscosity and surface tension. *Environ. Sci. Technol. Lett.* **2017**, *4*, 386-390.
- Liu, L.; Mishchenko, M. I.; Menon, S.; Macke, A.; Lacis, A. A. The effect of black carbon on scattering and absorption of solar radiation by cloud droplets. *J. Quant. Spectrosc. Radiat. Transfer.* **2002**, *74*, 195-204.
- Lohmann, U.; Feichter, J. Global indirect aerosol effects: a review. *Atmos. Chem. Phys.* **2005**, *5*, 715-737.
- Lockwood, D. J. Rayleigh and Mie scattering. *Encyclopedia of Color Science and Technology*, 1st ed.; Luo, M. R. ed.; Springer New York: New York, NY, 2016; pp. 1097-1107.
- McDonlad, J. E. Visibility reduction due to jet-exhaust carbon particles. *J. Appl. Meteorol.* **1962**, *1*, 391-398.
- McMurry, P. H.; Grosjean, D. Gas and aerosol wall losses in Teflon film smog chamber. *Environ. Sci. Technol.* **1985**, *19*, 1176-1182.
- Menon, S.; Hansen, J.; Nazarenko, L.; Luo, Y. Climate effects of black carbon aerosols in China and India. *Science.* **2002**, *297*, 2250-2253.
- Migliorini, F.; De luliis, S.; Cignoli, F.; Zizak, G. How “flat” is the rich premixed flame produced by your McKenna burner? *Combust. Flame.* **2008**, *153*, 384-393.
- Miracolo, M. A.; Hennigan, C. J.; Ranjan, M.; Nguyen, N. T.; Gordon, T. D.; Lipsky,

- E. M.; Presto, A. A.; Donahue, N. M.; Robinson, A. L. Secondary aerosol formation from photochemical aging of aircraft exhaust in a smog chamber. *Atmos. Chem. Phys.* **2011**, *11*, 4135-4147.
- Myhre, G.; Shindell, D.; Bréon, F.-M.; Collins, W.; Fuglestedt, J.; Huang, J.; Koch, D.; Lamarque, J.-F.; Lee, D.; Mendoza, B.; Nakajima, T.; Robock, A.; Stephens, G.; Takemura, T.; Zhang, H. Anthropogenic and natural radiative forcing. In *Climate Change 2013: The Physical Science Basis. Contribution of Working Group I to the Fifth Assessment Report of the Intergovernmental Panel on Climate Change*; Stocker, T.F.; Qin, D.; Plattner, G.-K.; Tignor, M. M.; Allen, S. K.; Boschung, J.; Nauels, A.; Xia, Y.; Bex, V.; Midgley, P. M., Eds.; Cambridge University Press: Cambridge, 2013; pp. 659-740.
- Nakao, S.; Tang, P.; Tang, X.; Clark, C. H.; Qi, L.; Seo, E.; Asa-Awuku, A.; Cocker III, D. Density and elemental ratios of secondary organic aerosol: Application of a density predication method. *Atmos. Environ.* **2013**, *68*, 273-277.
- Ng, N. L.; Kroll, J. H.; Chan, A. W. H.; Chhabra, P. S.; Flagan, R. C.; Seinfeld, J. H. Secondary organic aerosol formation from m-xylene, toluene, and benzene. *Atmospheric Chemistry and Physics Discussions*, European Geosciences Union, **2007**, *7*, 4085-4126.
- Olfert, J. S. A numerical calculation of the transfer function of the Fluted centrifugal particle mass analyzer. *Aerosol Sci. Technol.* **2005**, *39*, 1002-1009.
- Olfert, J. S.; Reavell, S. StJ.; Rushton, M. G.; Collings, N. The experimental transfer function of the Couette centrifugal particle mass analyzer. *J. Aerosol Sci.* **2006**, *37*, 1840-1852.
- Olofsson, N. -E.; Bladh, H.; Bohlin, A.; Johnsson, J.; Bengtsson, P, -E. Are sooting premixed porous-plug burner flames one-dimensional? A laser-based experimental investigation. *Combust. Sci. Technol.* **2013**, *185*, 293-309.
- Pu, Y.; Chen, J.; Wang, W.; Alfano, R. R. Basic optical scattering parameter of the brain and prostate tissues in the spectral range of 400-2400 nm. *Neurophotonics and Biomedical Spectroscopy.* **2019**, 229-252.

- Qiu, C.; Khalizov, A. F.; Zhang, R. Soot aging from OH-initiated oxidation of toluene. *Environ. Sci. Technol.* **2012**, *46*, 9464-9472.
- Queensland, c=A. U. o=T. S. of. Measuring visibility. <https://www.qld.gov.au/environment/pollution/monitoring/air/air-monitoring/measuring/aerosols#> (accessed Feb 19, 2020).
- Ramanathan, V.; Carmichael, G. Global and regional climate changes due to black carbon. *Nat. Geosci.* **2008**, *1*, 221-227.
- Redmond, H.; Thompson, J. E. Evaluation of a quantitative structure-property relationship (QSPR) for predicting mid-visible refractive index of secondary organic aerosol (SOA). *Phys. Chem. Chem. Phys.* **2011**, *13*, 6872-6882.
- Ruiz, P. A.; Lawrence, J. E.; Ferguson, S. T.; Wolfson, J. M.; Koutrakis, P. A counter-current parallel-plate membrane denuder for the non-specific removal of trace gases. *Environ. Sci. Technol.* **2006**, *40*, 5058-5063.
- Saathoff, H.; Naumann, K.-H.; Schnaiter, M.; Schöck, W.; Möhler, O.; Schurath, U.; Weingartner, E.; Gysel, M.; Baltensperger, U. Coating of Soot and (NH₄)₂SO₄ particles by ozonolysis products of α -pinene. *J. Aerosol Sci.* **2003**, *34*, 1297-1321.
- Schnaiter, M.; linke, C.; Möhler, K.-H. N.; Saathoff, H.; Wagner, R.; Schurath, U. Absorption amplification of black carbon internally mixed with secondary organic aerosol. *J. Geophys. Res.* **2005**, *110*, D19204.
- Schnitzler, E. G.; Dutt, A.; Charbonneau, A. M.; Olfert, J. S.; Jäger, W. Soot aggregate restructuring due to coatings of secondary organic aerosol derived from aromatic precursors. *Environ. Sci. Technol.* **2014**, *48*, 14309-14316.
- Schnitzler, E. G.; Gac, J. M.; Jäger, W. Coating surface tension dependence of soot aggregate restructuring. *J. Aerosol Sci.* **2017**, *106*, 43-55.
- Schwartz, J.; Laden, F.; Zanobetti, A. The concentration-response relation between PM_{2.5} and daily deaths. *Environ. Health Perspect.* **2002**, *110*, 1025-1029.
- Takemura, T.; Nozawa, T.; Emori, S.; Nakajima, T. Y.; Nakajima, T. Simulation of climate response to aerosol direct and indirect effects with aerosol

- transport-radiation model. *J. Geophys. Res.* **2005**, *110*, D02206.
- Tie, X.; Wu, D.; Brasseur, G. Lung cancer mortality and exposure to atmospheric aerosol particles in Guangzhou, China. *Atmos. Environ.* **2009**, *43*, 2375-2377.
- TSI Incorporated. Model 3771/3772 Condensation Particle Counter, Operation and Service manual. **2007**.
- TSI Incorporated. Model 3776 Ultrafine Condensation Particle Counter, Operation and Service manual. **2006**.
- TSI Incorporated. Series 3080 Electrostatic Classifier, Operation and Service manual. **2009**.
- Wang, R.; Tao, S.; Shen, H.; Huang, Y.; Chen, H.; Balkanski, Y.; Boucher, O.; Ciais, P.; Shen, G.; Li, W.; Zhang, Y.; Chen, Y.; Lin, N.; Su, S.; Li, B.; Liu, J.; Liu, W. Trend in Global Black Carbon Emissions from 1960 to 2007. *Environ. Sci. Technol.* **2014**, *48*, 6780-6787.
- Wu, S.; Lü, Z.; Hao, J.; Zhao, Z.; Li, J.; Takekawa, H.; Minoura, H.; Yasuda, A. Construction and characterization of an atmospheric simulation smog chamber. *Adv. Atmos. Sci.* **2007**, *24*, 250-258
- Xue, H.; Khalizov, A. F.; Wang, L.; Zheng, J.; Zhang, R. Effects of dicarboxylic acid coating on the optical properties of soot. *Phys. Chem. Chem. Phys.* **2009**, *11*, 7869-7875.
- Zhang, X.; McVay, R. C.; Huang, D. D.; Dalleska, N. F.; Aumont, B.; Flagan, R. C.; Seinfeld, J. H. Formation and evolution of molecular products in α -pinene secondary organic aerosol. *PNAS.* **2015**, *112*, 14168-14173.